

Fantastic Fits with fantasy of Active Galactic Nuclei Spectra - Exploring the Fe II emission near the H α line

DRAGANA ILIĆ,^{1,2} NEMANJA RAKIĆ,³ AND LUKA Č. POPOVIĆ^{4,1}

¹*Department of Astronomy, University of Belgrade - Faculty of Mathematics, Studentski trg 16, 11000 Belgrade, Serbia*

²*Humboldt Research Fellow, Hamburger Sternwarte, Universität Hamburg, Gojenbergsweg 112, 21029 Hamburg, Germany*

³*Physics Department, Faculty of Natural Sciences and Mathematics, University of Banjaluka, Mladena Stojanovića 2, 78000 Banjaluka, RS, Bosnia and Herzegovina*

⁴*Astronomical Observatory, Volgina 7, 11000 Belgrade, Serbia*

ABSTRACT

In this study, a refined approach for multicomponent fitting of active galactic nuclei (AGN) spectra is presented utilizing the newly developed Python code `fantasy` (fully automated python tool for AGN spectra analysis). AGN spectra are modeled by simultaneously considering the underlying broken power-law continuum, predefined emission line lists, and an Fe II model, which is here extended to cover the wavelength range 3700 - 11000 Å. The Fe II model, founded solely on atomic data, effectively describes the extensive emission of the complex iron ion in the vicinity of the H γ and H β lines, as well as near the H α line, which was previously rarely studied. The proposed spectral fitting approach is tested on a sample of high-quality AGN spectra from the Sloan Digital Sky Survey (SDSS) Data Release 17. The results indicate that when Fe II emission is present near H β , it is also detected redward from H α , potentially contaminating the broad H α line wings and thus affecting the measurements of its flux and width. The production of Fe II emission is found to be strongly correlated with Eddington luminosity and appears to be controlled by the similar mechanism as the hydrogen Balmer lines. The study highlights the benefits of fitting AGN type 1 spectra with the `fantasy` code, pointing that it may be used as a robust tool for analyzing a large number of AGN spectra in the coming spectral surveys.

Keywords: Active galactic nuclei(6) — Quasars(1319) — Atomic data(2216) — Spectral line lists(2082)

1. INTRODUCTION

Active galactic nuclei (AGN) spectra can be very complex, with underlying emission from the stellar component of the host galaxy, continuum emission predominantly from the accretion disk, and strong broad and narrow emission lines originating from regions at a wide range of distances from the central supermassive black hole (SMBH, see e.g. Netzer 2013). Disentangling the complex optical spectra of AGN is an important part of AGN research to understand the physical processes behind continuum and emission line production (Padovani et al. 2017). In addition, robust and reliable extraction of spectral parameters in type 1 AGN¹, such as the width and flux of the broad emission lines or the underlying continuum flux, is of importance for their application in estimating physical parameters such as the mass of the SMBH or the Eddington ratio (Shen et al. 2011; Liu et al. 2019). Both are needed to understand AGN and their role in galaxy evolution (e.g. Kormendy & Ho 2013). The two best known broad emission lines are the H β and H α lines, which are well studied and used for a large number of type 1 AGN (e.g., Greene & Ho 2005; Xiao et al. 2011; Shen et al. 2011; Liu et al. 2019; Rakshit et al. 2020).

Corresponding author: Dragana Ilić
dilic@matf.bg.ac.rs

¹ Type 1 AGN, also known as unobscured AGN, show broad emission lines in their UV, optical and NIR spectra.

We are still far from fully understanding the physical processes of the plasma in the broad line region (BLR), such as what the densities and temperatures are (Popović 2003; Marziani et al. 2020), and how to predict the observed emission line ratios (e.g., Ilić et al. 2012; Netzer 2020), and understand the production of diffuse BLR continuum emission (Chelouche et al. 2019), and the presence and role of dust (Baron et al. 2016; Czerny et al. 2022), or determine the location and origin of Fe II emission (e.g., Baldwin et al. 2004; Gaskell et al. 2022). For sure, the promising approach for these investigations is to exploit large spectral data sets and provide catalogues of their spectral properties, as has been done for more than half a million of quasars from the Sloan Digital Sky Survey (SDSS, Rakshit et al. 2020).

Some of the challenges in extracting pure broad H β and H α line profiles and measuring their spectral parameters, such as the full width at half maximum (FWHM) and line fluxes, lie in subtracting the contribution of the host galaxy stellar emission, estimating the underlying AGN continuum emission, and identifying and subtracting narrow and other satellite lines. This can be particularly difficult for type 1 AGNs with strong Fe II emitters, such as the narrow-line Seyfert 1 (NLSy1, see e.g., Rakshit et al. 2017; Paul et al. 2022). Contamination by Fe II is probably the most difficult to deal with. It is known that the complex Fe II ion generates thousands of line transitions (Wills et al. 1985; Sigut & Pradhan 1998, 2003; Sarkar et al. 2021). Therefore, these lines are typically blended and difficult to identify in AGN spectra, so there are several Fe II templates that can be used by the community (for recent review on different Fe II templates, see Park et al. 2022, and references therein). However, most templates do not focus on the region near the H α line, which can be contaminated by iron emission, especially in the line wings (Véron-Cetty et al. 2004).

Moreover, recent observations of the specific transient phenomena of stellar disruption in galactic nuclei, so-called tidal disruption events (TDEs, for a review see Gezari 2021) show that some of these events are strong Fe II emitters (Petrushevska et al. 2023). As pointed out in Frederick et al. (2021), misleading identification of emission line features can cause errors in the classification of these events. TDEs are becoming increasingly important because they provide a special opportunity to detect and study intermediate-mass black holes (Gezari 2022). With ongoing and upcoming large sky surveys that aim to explore the transient sky, such as Zwicky Transient Factory (ZTF Bellm et al. 2019) or Vera C. Rubin Legacy Survey in Space and Time (LSST Ivezić et al. 2019), the number of detected transients will increase rapidly, as will their spectroscopic-optical follow-up with either single campaigns or dedicated surveys, such as a very successful Public ESO Spectroscopic Survey for Transient Objects (PESSTO Smartt et al. 2015), the already accepted extragalactic community surveys² as a part of the 4-metre Multi-Object Spectrograph Telescope (4MOST de Jong et al. 2012), or the forthcoming Manuakea Spectroscopic Explore (MSE The MSE Science Team et al. 2019).

Hence, there is a need for software packages that can perform modelling, fitting, and analysis of AGN spectra in an automated manner. There are already a few publicly available codes, namely: i) Quasar Spectral Fitting package (QSFIT Calderone et al. 2017), an IDL based code for fitting all AGN emitting components simultaneously; ii) Python QSO fitting code (PyQSOFit Guo et al. 2018, 2019), designed for fitting quasar spectrum and additionally performs Monte-Carlo iterations using flux randomization to estimate uncertainties; iii) Sculptor, an interactive graphical user interface written in Python for general astronomical spectral analysis, with a special extension for quasar spectra (Schindler 2022). Nevertheless, other open-source packages are needed that are tailored to model optical AGN spectra and are easy to use. Here we use the recently developed Python code *fantasy* (Fully automated python tool for AGN spectra analysis Ilić et al. 2020; Rakić 2022), which is an updated approach to multicomponent fitting of AGN spectra. The main advantages of the code are: i) the ability to fit a wide range of wavelengths simultaneously (e.g., from H δ to H α), ii) the selection of lines from predefined line lists with the option to easily insert user-defined line lists, and iii) the flexibility to model a wide variety of type 1 AGN spectra. A special feature of the code is the use of the extended model of iron emission in the wavelength range 3700 – 11000 Å for which initial concepts were presented in Popović et al. (2004) and further developed in Kovačević et al. (2010).

Recently, during a transient event in an NLSy1 galaxy, the wavelength region redward from the H α line was heavily contaminated by iron emission (for details see Petrushevska et al. 2023). Most available iron templates focus on the H β region, since this line is most commonly observed in distant AGN and is widely used for SMBH mass estimates from single-epoch observations (for a review see Popović 2020). With new instruments focusing on the NIR spectrum, such as the James Web Space Telescope, observation of the H α line in distant quasars is becoming possible, and the need for more Fe II templates and models covering this wavelength band is evident. This has motivated us to investigate iron emission, which is known to exist in the vicinity of the H α line but has not yet been studied in detail except in

² <https://www.4most.eu/cms/science/extragalactic-community-surveys/>

Véron-Cetty et al. (2004). In addition, we will demonstrate the importance of simultaneously fitting the spectra of type 1 AGNs in a broader wavelength range, including emission line components along with the underlying continuum and Fe II emission model. We will investigate the physical properties of regions emitting broad lines, with particular attention to the Fe II emission near the H α line. For this purpose, we use a selection of optical spectra of type 1 AGN obtained from the public database of the SDSS latest Data Release 17³, as well as as the publicly available optical spectra of I Zw 1, a well-known NLSy1, typically used to demonstrate the suitability of iron templates in AGN.

The paper is organized as follows. In Sect. 2, we describe the data set used. In Sect. 3 we present our extended semi-empirical model of Fe II emission and describe the main functionalities of `fantasy` code, whereas in Sect. 4 we present the results and provide relevant discussion. Finally, in Sect. 6 we list our conclusions. We assume a cosmology with $H_0 = 67 \text{ km s}^{-1} \text{ Mpc}^{-1}$, $\Omega_m = 0.32$ and $\Omega_\Lambda = 0.68$ to calculate the luminosity distance to studied objects.

2. DATA SAMPLE

We select a sample of type 1 AGN from the latest SDSS Data Release 17 (DR17, Abdurro’uf et al. 2022), where we specify as selection criteria the high signal-to-noise ratio of the optical spectra ($S/N > 35$) and the redshift $z < 0.4$. The first criterion excludes the presence of noisy spectra that may significantly bias the modelling of complex AGN spectra, especially iron emission. The second criterion ensures that both H β and H α are included. The DR17 is a fourth data release from the fourth phase of the survey (SDSS-IV), which contains the complete data set of optical single-fibre spectroscopy of the SDSS⁴ through January 2021 (Smee et al. 2013). The selection process and the characteristics of the selected sample are the same as in Rakić (2022), who used DR16 data (Ahumada et al. 2020). The query yielded 676 objects, of which 21 were discarded either because H α emission was absent or distorted, or objects were misclassified as type 1 AGN while they are rather type 2 as no broad component is seen. The remaining 655 SDSS AGN type 1 objects were further investigated (referred to as the SDSS sample).

One way to represent the distribution of type 1 AGN is to use a quasar main sequence diagram, defined with FWHM H β - R_{FeII} ⁵ space (Sulentic et al. 2000; Shen & Ho 2014; Du et al. 2016; Marziani et al. 2022). These studies have shown that R_{FeII} emission is a proxy for accretion strength in AGN, roughly also indicated by the Eddington ratio (see also Dong et al. 2011). The quasar main sequence is mainly occupied by two large groups of objects, populations A and B, defined according to the full width at half maximum (FWHM) of H β line (e.g., Sulentic et al. 2000, 2002; Marziani et al. 2022). These two populations have different physical properties and possibly different orientation (Marziani et al. 2018a, 2022). Population B objects have broader emission lines ($\text{FWHM} \geq 4000 \text{ km s}^{-1}$), higher inclination angle, low Eddington ratio, and weak Fe II emission ($R_{\text{FeII}} \leq 0.5$), whereas population A, occupying the other side of the diagram, have narrower broad emission lines, lower inclination, higher Eddington ratio, and strong Fe II (see a recent review Marziani et al. 2022). The extreme end of the objects of population A, which show very strong iron emission ($R_{\text{FeII}} > 1$), are also of great interest (Marziani et al. 2022).

Following the above, our SDSS sample of 655 objects was divided into 362 objects from population A (referred to as the “pop A” sample in the remainder of this text) and 293 objects from population B (“pop B” sample). A subset of 105 objects from the pop A sample belongs to the so-called extreme population A ($R_{\text{FeII}} > 1$). This sample is treated separately and we refer to it as the “xA” sample. Fig. 1 presents the distributions of the selected SDSS sample with the cosmological redshift z (upper panel) and continuum luminosity at 5100 Å (lower panel), shown as stacked bars of pop A (red) and pop B (green) sub-samples. All samples (total, pop A, pop B) are almost uniformly distributed across the redshift, showing a slight decrease towards higher redshift (seen also in Liu et al. 2019, who studied a sample of type 1 AGN with redshift < 0.35). The continuum luminosity distribution is asymmetric toward higher-luminosity, which is typical for type 1 AGN from SDSS (Liu et al. 2019), with most objects (95%) in the range $\log(L_{5100}) = [42.5\text{-}45.3] \text{ erg s}^{-1}$, with the median of 44.3.

To demonstrate the importance of simultaneous multi-component fitting of AGN spectra, in particular to extract Fe II emission, we also test spectral fitting on a publicly available optical spectrum of the well-known NLSy1 I Zw1 (taken from Tsuzuki et al. 2006)⁶, which is widely used to construct and test templates and models of Fe II emission in AGN.

³ <https://www.sdss4.org>

⁴ www.sdss.org/dr17/spectro/

⁵ R_{FeII} is a measure of the Fe II optical emission, defined as the ratio of the equivalent widths of Fe II emission in the wavelength range 4435–4685 Å and H β broad line.

⁶ A spectrum was retrieved via the NASA/IPAC Extragalactic Database (NED), <https://ned.ipac.caltech.edu>, see also <http://www.ioa.s.u-tokyo.ac.jp/~kkawara/quasars/>.

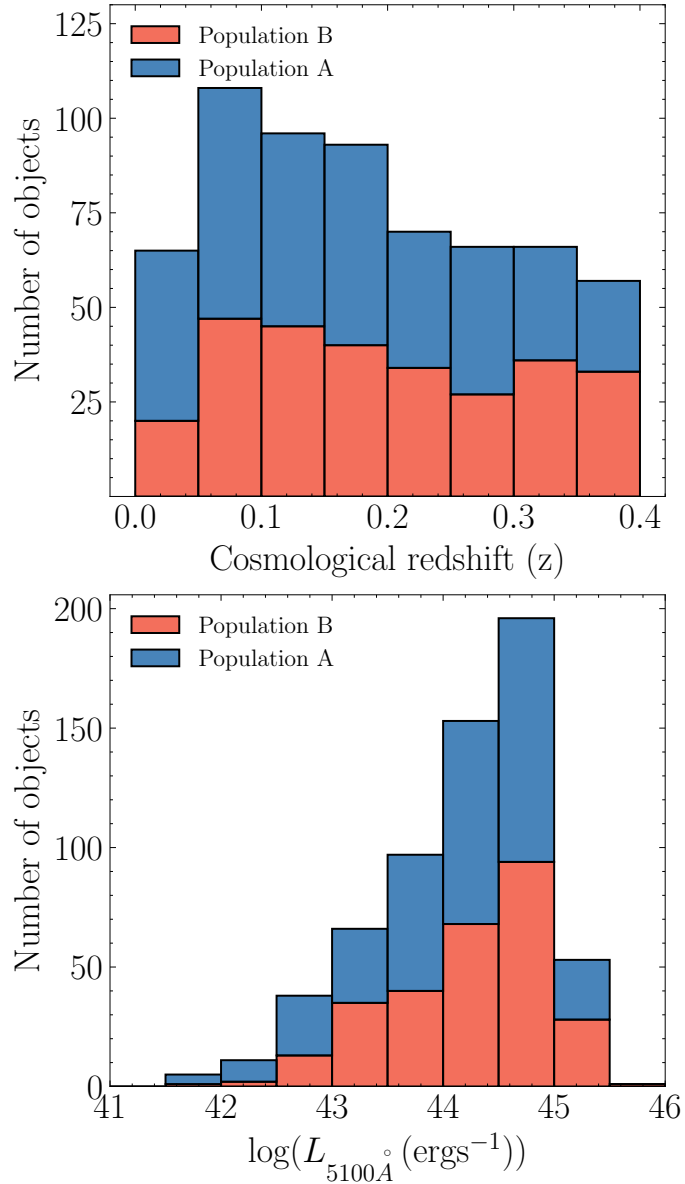


Figure 1. Distribution of SDSS sample of 655 objects with the cosmological redshift (upper panel) and continuum luminosity at 5100 Å (bottom panel) presented with stacked bars of pop A (red) and pop B (blue) sub-samples.

3. METHODS AND ANALYSIS

In this section we present the approach to modeling the complex spectra of type 1 AGN using the code `fantasy` and the description of the extended Fe II emission model.

3.1. Extension to the atomic model of Fe II emission

For interpreting the emission within the type 1 AGN spectra, one important requirement is to carefully reconstruct the Fe II emission. In addition, understanding the origin of the strong emission of a complex ion of one-time ionized iron in AGN is a continuing quest (e.g., Netzer 1980; Penston 1987; Verner et al. 1999; Sigut et al. 2004; Panda et al. 2019; Sarkar et al. 2021; Gaskell et al. 2022). Fe II emission is present in a broad spectral range and typically contaminates other broad lines from the UV (e.g., Mg II line Vestergaard & Wilkes 2001; Popović et al. 2019), through optical (e.g., H β and H α lines Véron-Cetty et al. 2004; Park et al. 2022) to near-infrared bands (e.g., Pa γ line Rudy et al. 2000; Landt et al. 2008; Garcia-Rissmann et al. 2012; Marinello et al. 2016). Their investigations are important for understanding the physics of the broad line region.

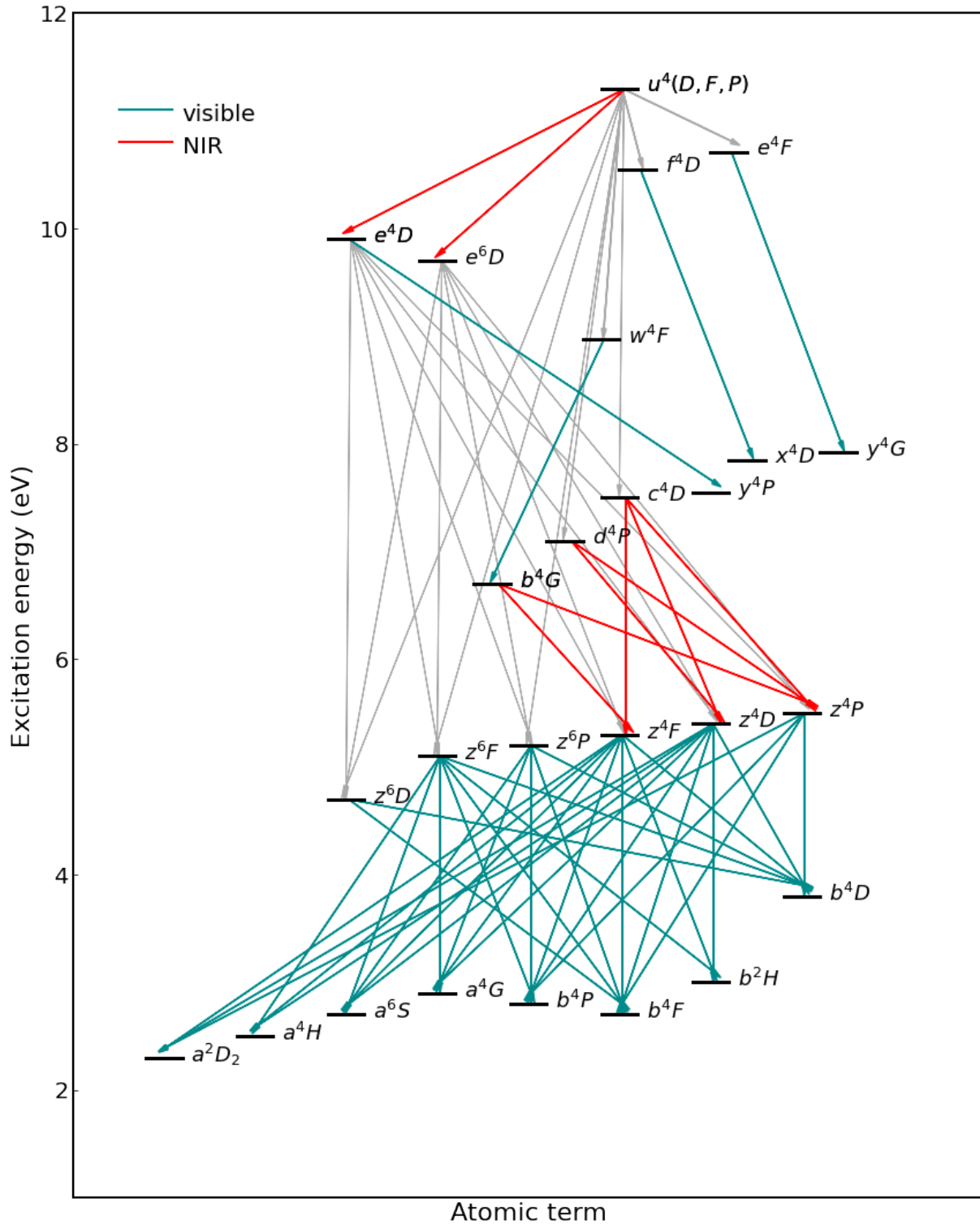


Figure 2. Partial Grotrian diagram for Fe II, showing the transitions considered in the presented model of Fe II emission in the wavelength range 3700-11000 Å. The upper levels $u^4(D, F, P)$ are populated by Ly α photons, from which the cascades to lower levels are shown: red lines show the NIR transitions (bumps at 9200 Å and 1 μ m) and dark cyan lines represent the transitions in the optical band (centered at 4570 Å and 5270Å which are the two strongest bumps around H β). The gray lines represent the transitions responsible for populating the upper levels, mainly through UV emission, to illustrate the path.

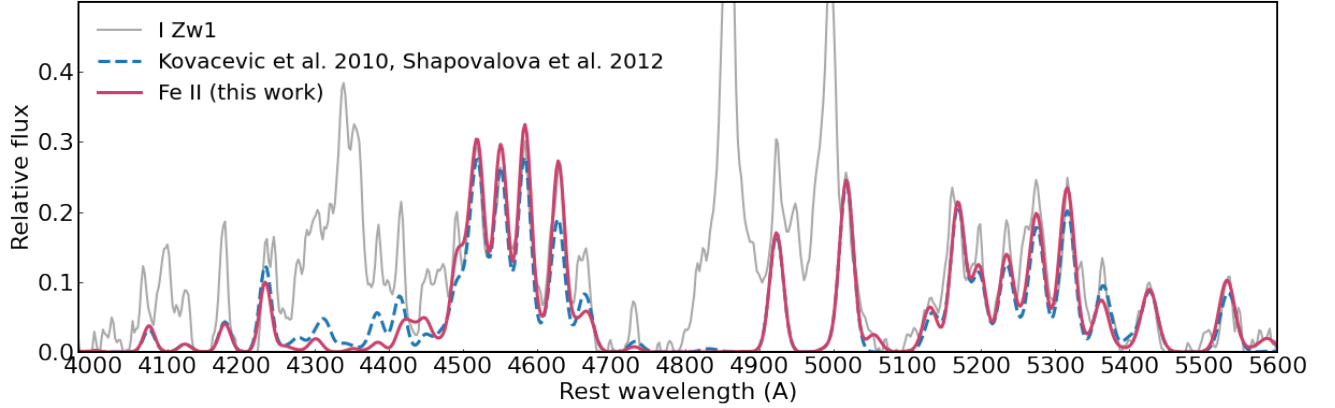


Figure 3. Comparison of the semi-empirical Fe II model presented in [Kovačević et al. \(2010\)](#) and [Shapovalova et al. \(2012\)](#) with the model of Fe II emission presented in this work, which relies solely on the atomic data.

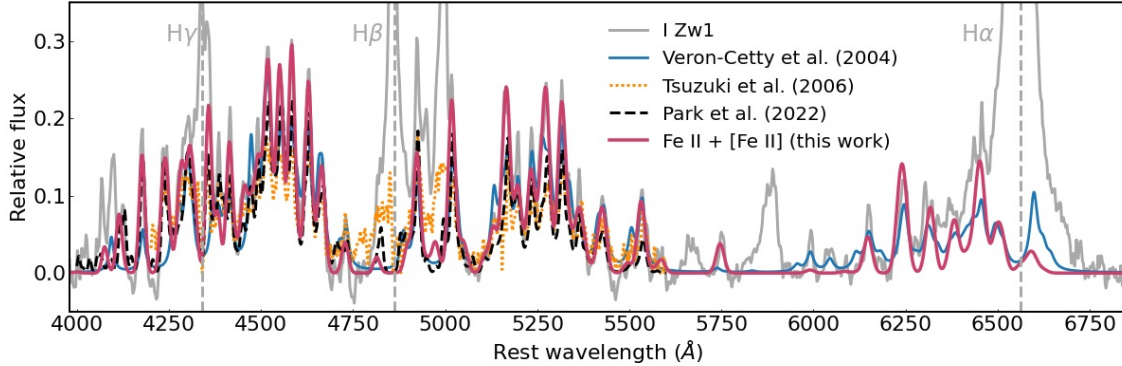


Figure 4. Different Fe II templates compared to the I Zw 1 spectrum from which the continuum emission was subtracted. The Fe II model presented here is the result of fitting the observations and also includes [Fe II] lines that are strong in this object (see Section 3.2.1 for details).

Usually, iron emission is modeled with empirical templates ([Boroson & Green 1992](#); [Vestergaard & Wilkes 2001](#); [Véron-Cetty et al. 2004](#); [Tsuzuki et al. 2006](#); [Park et al. 2022](#)). These templates consider that the relative intensities of identified Fe II lines are proportional to empirical ratios measured in AGN spectra whose broad lines are narrow enough, so that the Fe II features are more easily separated from other emission lines, i.e. NLSy1. Some Fe II templates are governed by the identification of emission lines within the same important multiplets ([Marinello et al. 2016, 2020](#)). The semi-empirical approach to modelling the Fe II emission was presented in [Kovačević et al. \(2010\)](#) and updated in [Shapovalova et al. \(2012\)](#). Their semi-empirical model covers the wavelength range 4000 - 5500 Å, and is mainly based on the atomic parameters of the strongest iron transitions. In short, the model consists of Fe II line-sets grouped according to the same lower energy level in the transition with line intensities connected by the line transition oscillatory strengths, for a given excitation temperature, usually assumed to be 10^4K . For few line groups, the relative line intensities were measured from I Zw 1 ([Kovačević et al. 2010](#)), which made this model a semi-empirical one. For a detailed presentation of most relevant Fe II templates, their properties, applications, and comparisons, we refer to the recent review presented in [Park et al. \(2022\)](#). It is worth noting that given the complex energy level structure of the Fe II ion and a huge number of transitions producing rich spectrum in the UV, optical and NIR regions, it remains challenging to use in practice fully theoretical Fe II templates (such as [Sigut & Pradhan 2003](#); [Bruhweiler & Verner 2008](#)). We emphasize again that most Fe II templates focus on the H β region, which is the most studied broad emission line in AGN.

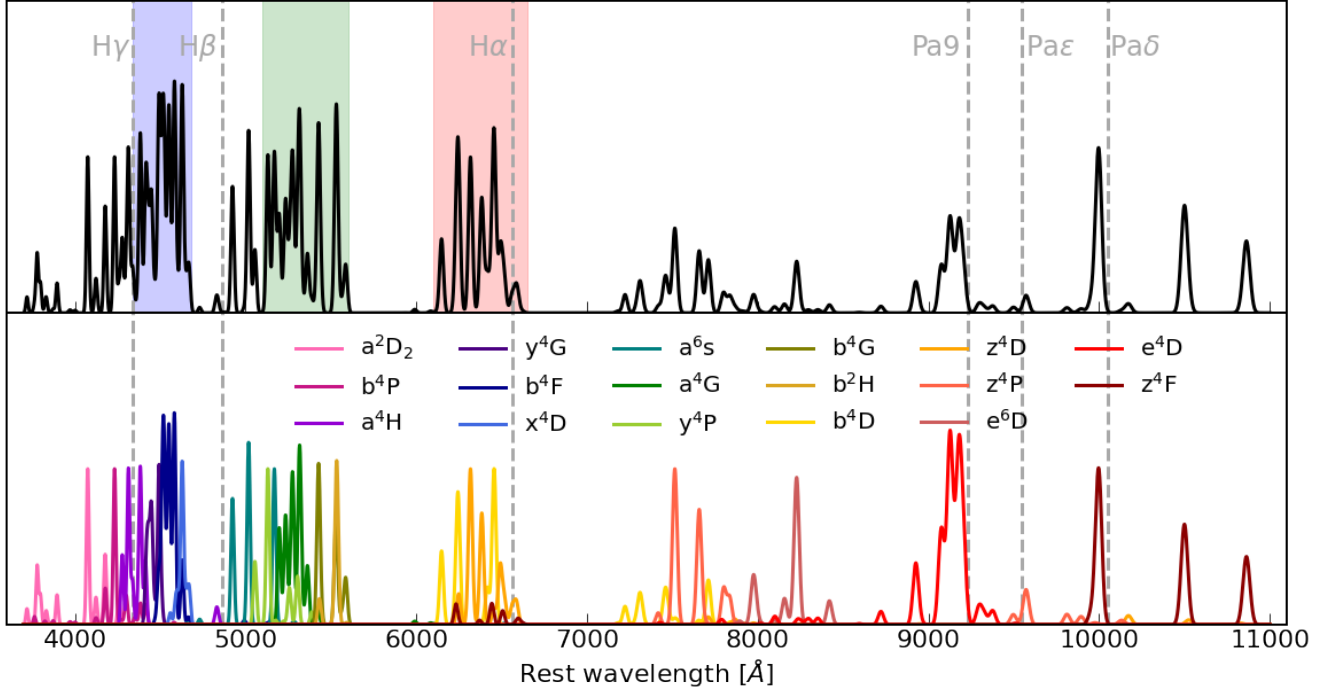


Figure 5. Fe II model in the wavelength range 3700 - 11000 Å, with atomic groups indicated in the bottom panel. The position of the hydrogen Balmer and Paschen series are also indicated with the dashed vertical lines, whereas the shaded areas indicate the position of iron bands used later in the analysis: Fe II blue (4340–4680 Å), Fe II green (5100–5600 Å), and Fe II red (6100–6650 Å).

Table 1. Example of Fe II transitions used in the model for the lower level a^6S (energy 2.891 eV) group with the reference line set to a relative intensity of 1.000.

Wavelength (air)	log(gf)	transition	E(low)	E(up)	Relative	Ref.
Å		lower – upper	eV	eV	intensity	
4593.83	-4.923	$a^6S_{5/2} - z^4F_{5/2}$	2.891	5.589	0.000	(3)
4601.38	-4.428	$a^6S_{5/2} - z^4D_{3/2}$	2.891	5.585	0.001	(3)
4656.98	-3.630	$a^6S_{5/2} - z^4D_{5/2}$	2.891	5.553	0.007	(3)
4663.71	-3.820	$a^6S_{5/2} - z^4F_{7/2}$	2.891	5.549	0.004	(1)
4731.45	-2.921	$a^6S_{5/2} - z^4D_{7/2}$	2.891	5.511	0.035	(2)
4923.93	-1.561	$a^6S_{5/2} - z^6P_{3/2}$	2.891	5.408	0.810	(2)
5018.44	-1.400	$a^6S_{5/2} - z^6P_{5/2}$	2.891	5.361	1.170	(2)
5169.03	-1.466	$a^6S_{5/2} - z^6P_{7/2}$	2.891	5.289	1.000	(2)
5256.94	-4.250	$a^6S_{5/2} - z^6F_{5/2}$	2.891	5.249	0.002	(3)
5284.11	-3.121	$a^6S_{5/2} - z^6F_{7/2}$	2.891	5.237	0.022	(2)
6369.46	-4.253	$a^6S_{5/2} - z^6D_{3/2}$	2.891	4.837	0.001	(3)
6432.68	-3.708	$a^6S_{5/2} - z^6D_{5/2}$	2.891	4.818	0.005	(3)
6516.08	-3.450	$a^6S_{5/2} - z^6D_{7/2}$	2.891	4.793	0.009	(3)

NOTE—Columns give line transition wavelength in air (in Å), oscillatory strength, the configuration of lower and upper energy level, corresponding energies (in eV), and a relative intensity with respect to the reference line, where intensity is set to 1.000. References for the used oscillatory strength: 1 - (Fuhr et al. 1981), 2 - (Kovačević et al. 2010), 3 - atomic database (<https://lweb.cfa.harvard.edu/amp/ampdata/kurucz23/sekur.html>). Table 1 is published in its entirety in the machine-readable format. A portion is shown here for guidance regarding its form and content.

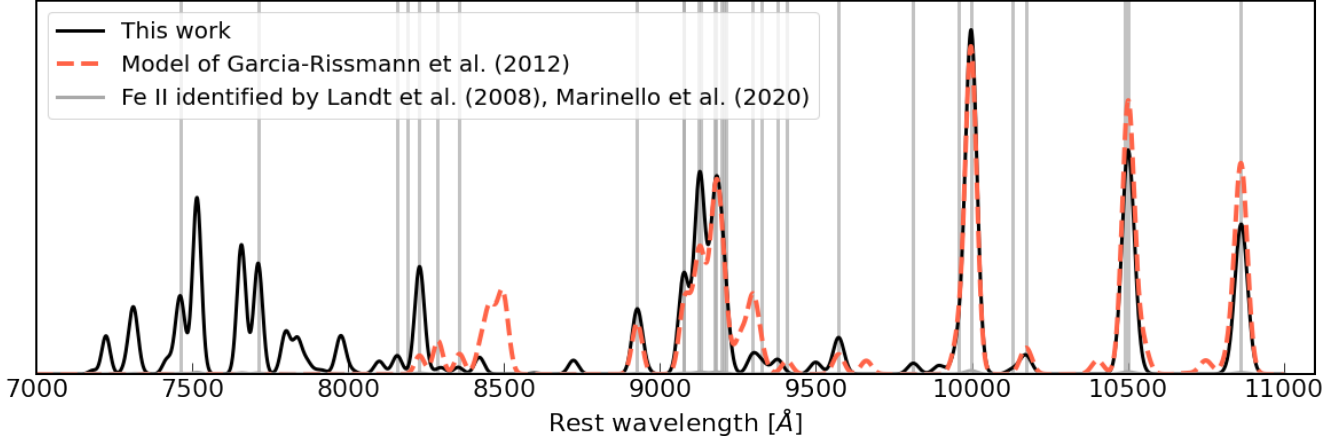


Figure 6. Comparison of the Fe II model (black solid line) in the wavelength range 7000 - 11000 Å, with the Fe II model provided for the wavelength range 8200 - 11400 Å in Garcia-Rissmann et al. (2012) (red dashed line, see text for details). The position of Fe II line identified in Landt et al. (2008); Marinello et al. (2020) are marked with vertical lines.

In this work, our main motivation was to develop the Fe II model that is extended to include the $H\alpha$ line region, which is also strongly populated by Fe II lines in NLSy1 objects (e.g., Tsuzuki et al. 2006; Dong et al. 2011; Park et al. 2022), and could be important in transient event, such as TDEs (see Petrushevska et al. 2023, and reference therein). Therefore, based on the same approach and assumptions presented in Kovačević et al. (2010), here we construct the Fe II model in the 3700 - 11000 Å wavelength range. In addition, here we revise the group of so-called high-excitation lines, for which the line ratios have been measured from I Zw 1 spectrum in Kovačević et al. (2010). It follows that the proposed model of Fe II is based solely on atomic data and the assumed excitation temperature. The individual line profiles in this model of Fe II are assumed to be Gaussians with the same width and shift. The lines are grouped to have the same lower level of transition, and all lines in a single group have a fixed intensity (calculated from the atomic data) relative to the strongest line in the atomic group. This leaves only the intensities of the strongest lines as free parameters. It has been long known that various Fe II optical multiplets do not have the same relative intensities in different objects (see e.g., van Groningen 1993; Véron-Cetty et al. 2004; Park et al. 2022). This multi-component model of Fe II emission has been shown to provide more flexibility for precise and careful fitting of diverse AGN spectra than monolithic empirical templates with a single overall intensity (see e.g., the observations and analysis in Kovačević et al. 2010; Shapovalova et al. 2012; Kovačević-Dojčinović & Popović 2015; Popović et al. 2019), where only the line width and shift are varied. In the following, we describe how the most important atomic transitions were selected for each atomic group.

We consider the possible path of electron transitions within the Fe II ion. In addition to the collisional excitation as one of the important mechanisms for the production of strong optical Fe II emission (Garcia-Rissmann et al. 2012; Marinello et al. 2016), it has been discussed that the $Ly\alpha$ fluorescence is another relevant process for populating upper levels of Fe II (Penston 1987; Sigut & Pradhan 1998, 2003; Sarkar et al. 2021), and thus responsible for NIR Fe II emission, and later contributing to the optical Fe II to a level of at least 20% (as shown in Garcia-Rissmann et al. 2012; Marinello et al. 2016). We start from the upper levels $u^4(D,F,P)$, which may be populated with $Ly\alpha$ photons (Figure 2). From these, photons cascade down through transitions in the NIR (see Table 1), as also discussed and illustrated in Sigut & Pradhan (2003); Marinello et al. (2016, 2020). These two groups of upper levels are responsible for populating the upper levels in the energy range of 4–7 eV through UV transitions (the Fe II emission in UV will be studied elsewhere). These are the known energy levels previously identified by Kovačević et al. (2010); Shapovalova et al. (2012); Véron-Cetty et al. (2004) which give rise to two main optical Fe II bumps around $H\beta$ line centered at 4570 Å and 5270 Å (indicated with dark cyan lines in Fig 2). We group the lines based on the same lower level of the transition, so that the line intensities are constrained only by the transition oscillatory strength f , which are listed gf in Table 1, where g is the level statistical weight. As an example, Table 1 lists the transitions identified within the a^6S group, and the complete list with all transitions is available in a machine-readable format in the online Journal.

In selecting transition groups in the wavelength range near the $H\alpha$ line and beyond, we were guided by the Fe II transitions previously identified as strong, relying primarily on the work of Véron-Cetty et al. (2004); Park et al.

(2022) for the optical Fe II and Rudy et al. (2000); Garcia-Rissmann et al. (2012); Marinello et al. (2020) for the NIR Fe II. Only the lines with oscillatory strength ($\log(gf) > -5$) were selected. The oscillatory strengths were adopted from Kovačević et al. (2010) and Shapovalova et al. (2012), whereas for the new transition groups they were taken from the atomic spectral line database from R. L. Kurucz⁷. In several cases we have updated $\log(gf)$ from the values given in Fuhr et al. (1981) as they have been shown to give line ratios that better describe the observations. The reference from which oscillatory strengths were taken is also given in Table 1. For the calculation of the line ratios, we used the excitation temperature of 10^4 K, which has been shown to represent well the region where these lines arise (Sulentic et al. 2000; Ilić et al. 2012). The line ratios would not change significantly for small variations of excitation temperature (Kovačević et al. 2010).

We outline two important updates with respect to the semi-empirical Fe II model presented in Kovačević et al. (2010), and further extended in Shapovalova et al. (2012):

1. The wavelength range was extended to cover 3700 – 11000 Å, whereas originally it was focused on 4200 - 5600 Å because this region around the H β line was the most studied.
2. Instead of using so-called high-excitation lines (see discussion in Kovačević et al. 2010, and their Table 3), whose ratios were previously measured from I Zw 1 spectrum, we have revised the list and assembled them into four atomic groups: y⁴G, b⁴G, x⁴D, y⁴P, as shown in Fig. 2. These groups are coming from the high-energy levels that are populated through the same paths as other levels (Fig. 2). The strongest lines in these groups were also identified by Kovačević et al. (2010) (see their Table 3) and Véron-Cetty et al. (2004).

This makes it a full model of Fe II emission that relies only on the atomic data. It contains a total of 283 transitions, divided into 17 atomic groups, in the wavelength range of 3700 – 11000 Å (line transitions are listed in Table 1 and shown in Fig. 2 and 5, bottom panel). In comparison, the previous semi-empirical model had 57 line transitions in the 4200 – 5600 Å, now the same range contains 125 transitions. However, the number of free parameters used in the fits has remained the same. Most of these lines are much weaker (see Table 1), but these are all included since in iron-rich objects their contribution may not be negligible, and they do not burden the computation (see Section 3.2 for details on modeling). Nevertheless, the extended model of Fe II emission differs only slightly from the original semi-empirical of Kovačević et al. (2010) model as shown in Fig. 3.

Figure 4 presents some widely used Fe II templates taken from the literature that are compared to the I Zw 1 spectrum, from which the continuum emission has been subtracted. The Fe II model presented in this paper is a result of the multi-component fitting (described in Section 3.2) and includes also [Fe II] lines which are strong in this and other similar iron-rich AGN. Full Fe II model in the wavelength range 3700 - 11000 Å is presented in Fig. 5 with 17 atomic groups indicated on the bottom panel with different color. All lines are set to have a width of 1300 km s⁻¹, with intensities of reference lines arbitrary selected.

In Figure 6 we zoom in the NIR part of the Fe II model in the wavelength range 7000 - 11000 Å. There is not much work dedicated to building the Fe II templates in NIR, mostly due to the observational limitation to obtain NIR spectra for distant AGN. In selecting the most dominant line transitions, we were governed by so-called well-known “1 μ m” Fe II features at λ 9997, λ 10501, and λ 10863 (Rudy et al. 2000). We compare the proposed model with the Fe II model provided for the wavelength range 8200 - 11000 Å by Garcia-Rissmann et al. (2012) (Fig. 6, red dashed line), compiled from their best model for I Zw 1 (see their Tables 2 and 3). Fe II line identified in Landt et al. (2008); Marinello et al. (2020) are also marked with vertical lines. In this work, we focus on the spectra in 4000-7000Å wavelength range due to the availability of SDSS spectra in this domain. The properties of 221 NIR iron emission in AGN spectra and further testing of the proposed model will be investigated in detail in a forthcoming publication.

3.2. AGN spectral fitting

For the modeling of AGN spectra, here we rely on the open-source code `fantasy` (Fully Automated pythoN Tool for AGN Spectra analySis)⁸. This is a python-based code for multi-component spectral fitting, optimized for type 1 AGN spectra in the wavelength range 3700-11000 Å, already successfully used in several studies (Ilić et al. 2020; Rakić 2022; Petrushevska et al. 2023). The AGN spectra are modeled simultaneously with the underlying broken power-law continuum, the predefined emission line lists, and the Fe II model. The code is flexible in the selection of different

⁷ <https://web.cfa.harvard.edu/amp/ampdata/kurucz23/sekur.html>

⁸ <https://fantasy-agn.readthedocs.io>

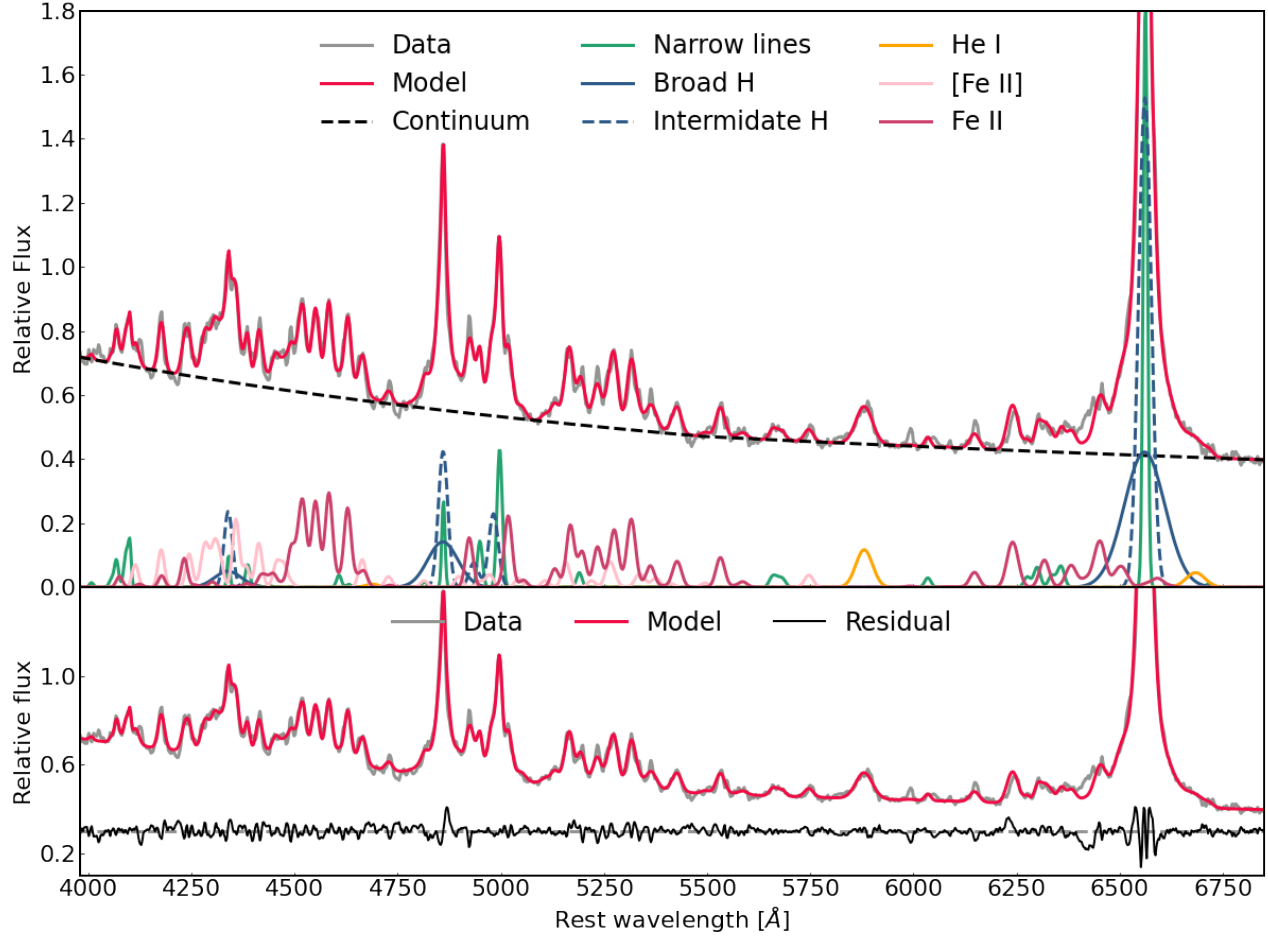


Figure 7. Multi-component fitting with the `fantasy` code of the I Zw 1 observed spectrum (gray line) in the $\lambda\lambda 4000\text{--}6800$ Å wavelength region. The model (red line) consists of: broken power-law (black dashed line), narrow lines (green solid line), broad (blue solid line) and intermediate (blue dashed line) components of Balmer lines: $H\alpha$, $H\beta$, $H\delta$, He I lines (yellow line), intermediate components of [O III] (blue dashed line), and Fe II model (dark-red line) and [Fe II] lines (light-red line). Bottom panel shows the zoomed-in observed (gray line), model (red line), and residual spectrum (black line).

groups of lines, either already predefined lists (e.g., standard narrow lines, Hydrogen and Helium lines, Fe II model, etc), but gives full flexibility to the user to merge predefined line lists or create customized line list. Fitting is based on Levenberg–Marquardt algorithm implemented through `sherpa`⁹ python package (Burke et al. 2022). We describe below the most important features of the `fantasy` code used in this analysis:

1. Several pre-processing steps to prepare the AGN spectra for multi-component fitting are available, such as the Galactic extinction and cosmological redshift correction. Based on either data provided in the header or manually inserted, the spectra are corrected for Galactic extinction using dust map data from Schlegel et al. (1998), and for the cosmological redshift.
2. To estimate and subtract the contribution of the host-galaxy starlight, we have decided for the approach already tested and used for SDSS spectra (Rakshit et al. 2020), which shows that most AGN spectra can be reconstructed as a linear combination of galaxy and quasar eigenspectra. Using the Principle Component Analysis, Yip et al. (2004a,b) constructed from 170,000 galaxy SDSS spectra and 16,707 quasar SDSS spectra, a set of galaxy and quasar eigenspectra. Vanden Berk et al. (2006) showed that the majority of AGN spectra can be reconstructed

⁹ <https://pypi.org/project/sherpa/>

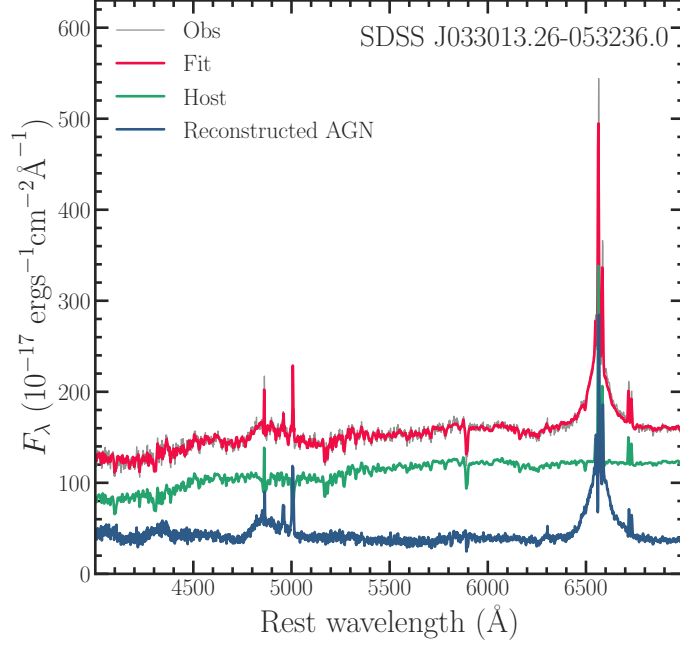


Figure 8. An example of the AGN component (blue line) reconstructed after subtracting the contribution of the stellar component of the host galaxy (green line) from an observed spectrum (gray line) of SDSS J033013.26-053236.0. The host-galaxy emission contributes on the level of 76% to the observed continuum flux around 6000 Å

using the linear combination of 10 quasar eigenspectra from Yip et al. (2004b) and 5 galaxy eigenspectra from Yip et al. (2004a) as

$$F(\lambda) = \sum_0^{10} a_i q_i(\lambda) + \sum_0^5 b_i h_i(\lambda) \quad (1)$$

where $F(\lambda)$ is observed spectra, a_i , and b_i are linear coefficients and q_i and h_i are quasar and galaxy eigenspectra, respectively. Note that prior to the fitting, the observed and eigenspectra are binned to the same spectral resolution and wavelength range. Optionally, `fantasy` may use all available eigenvectors (10 eigenvectors for galaxy (stellar) and 15 for quasar components, Yip et al. 2004a,b). In this case the code will test for different number of components until reaching the best result based on the χ^2 parameter. In both cases, the weighted fit is used in order to avoid accounting for strong emission lines, with an option to mask strong narrow emission lines. By subtracting the reconstructed host galaxy contribution from the observed spectrum, one can obtain the pure AGN spectrum. The proposed technique allows for the recovery of the host galaxy spectrum, which is not resolved otherwise, which enables some studies of host galaxy properties, such as type, luminosity, colors, stellar mass, star-formation rates, etc. (see Vanden Berk et al. 2006).

3. One challenging step in bulk fitting of AGN spectra with different spectral features is the identification of emission lines and features present. `fantasy` approaches this by creating predefined standard lists of AGN emission lines within the specified wavelength range, such as: Hydrogen lines (Balmer and Paschen series), Helium lines (both He I and He II), most present narrow emission lines ([O III], [N II]), other AGN narrow lines (e.g., [S II], [O I]), other AGN broad lines (Ca I, O I), coronal lines (e.g. [Fe X], [Ar V]), Fe II model (described in Section 3.1), etc. In case of very strong Fe II emitters, such as NLSy1 galaxies, sometimes it is necessary to include additional transitions from forbidden Fe II (see e.g., Véron-Cetty et al. 2004). Users can modify available line lists, as well as create completely new ones. All identified line lists are available (Table 3 in the Appendix) for completeness, as we found that not much on this aspect is provided in the literature.
4. Many works use a standard approach and fit the optical continuum in AGN with a single power-law with adjustable spectral index (e.g. Rakshit et al. 2020). However, in order to be able to simultaneously fit the continuum and emission line features in a wider range of wavelengths (i.e., to cover both H α and H β lines),

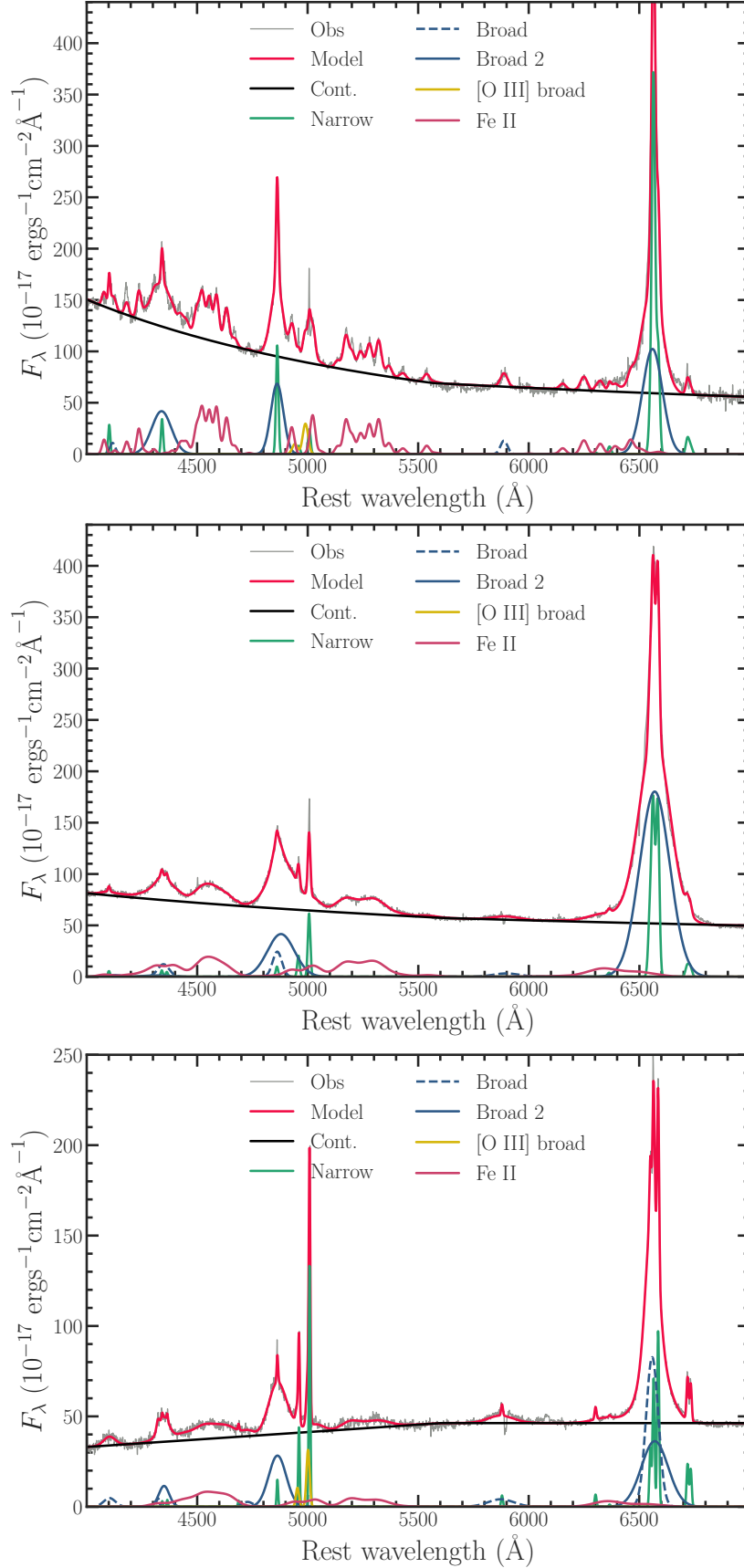


Figure 9. The same as in Figure 7 but for three cases of host-galaxy corrected spectra from SDSS sample with diverse spectral properties to illustrate the *fantasy* multi-component fittings: SDSS J010226.31-003904.5 (upper), SDSS J094620.86+334746.9 (middle) and SDSS SDSS J093641.05+101415.9 (bottom). All components used in the fitting model (broken power-law continuum and emission line features) are indicated with different colors (see text for details).

we have decided to go for more flexibility and use broken power-law (Dong et al. 2008). Vanden Berk et al. (2001) detected in a composite SDSS spectrum an abrupt change in the continuum slope redward from H β line (see their Figure 5), and discussed that the stellar light from the host galaxies may cause the steepening of the spectral index beyond 5000 Å, but also pointed that it could be a real change in the quasar continuum, caused by the tail-end of thermal emission from hot dust. Liu et al. (2019) demonstrated that for SDSS type 1 AGN, the broken power-law with a break wavelength of ~ 5650 Å, is well suited for a simultaneous fit of continuum and emission lines. The break wavelength of 5650 Å is adopted because it can ideally avoid the wavelength regions of the prominent emission lines. Therefore, the `fantasy` code uses a more generalized approach with the broken power-law for representing the AGN continuum, with the option to define the break wavelength, depending on the wavelength range of interest.

5. Final step is the spectral model construction and fitting. Basic model for AGN spectra should contain an underlying continuum (generalized to be in the form of a broken power-law) and narrow and broad emission lines. Depending on the wavelength range, spectral quality (S/N ratio, spectra resolution), and object type, the fitting model can be customized to contain many and complex emission features. Special feature in `fantasy` is a possibility to create a “fixed model”, which calls all lines from the indicated line list(s) and sets them to have the same width and shift. An option to create a “tide model” includes all lines in indicated lists to have width and shift tided to the reference line (this is typically strong narrow [O III] $\lambda 5007$ line). Creating a “fei model” calls for the Fe II model, in which all iron lines have the same width and shift, and line intensity ratios are calculated as described in Section 3.1. All emission lines are modeled with Gaussian function, defined with shift, width, and intensity.
6. The uncertainties in the spectra, and consequently in measured spectral quantities were estimated using a Monte Carlo approach (see e.g. description in Rakshit et al. 2020). We created 50 mock spectra for each object in the sample, by adding Gaussian random noise to the original spectrum at each pixel. The same fitting model was applied to all mock spectra as was done for the original one. Spectral quantities of interest (flux, line widths and shifts) were estimated from the original and mock spectra, giving us the distribution of each spectral quantity. For the uncertainty we then take the semi-amplitude of the range enclosing the 16th and 84th percentiles of the distribution.

3.2.1. Case of I Zw 1

To illustrate the potential of the `fantasy` code, the multi-component fitting was done on the I Zw 1 observed spectrum in the $\lambda\lambda 4000\text{--}6800$ Å wavelength region (Fig. 7), which was corrected for Galactic extinction. We note that the I Zw 1 spectrum is pretty flat in the blue part, indicating that there might be significant intrinsic extinction by the host-galaxy (see Richards et al. 2006; Park et al. 2022). We have tested the host galaxy subtraction provided in `fantasy` (see Section 3.2), and seen no noticeable difference in the corrected spectrum in the region of interest (near H α and H β line), and consequently in Fe II fittings, so we continued the analysis on the I Zw 1 spectrum not corrected for the host-galaxy contribution. The model (red line) consists of: broken power-law (black dashed line), narrow lines (green solid line), broad (blue solid line) and intermediate (blue dashed line) components of Balmer lines: H α , H β , H δ , He I lines (yellow line), intermediate components of [O III] (blue dashed line), and Fe II model (dark-red line) and [Fe II] lines (light-red line). All lines within each modelling component are set to have the same width and shifts. We note here that since I Zw 1 and other NLSy1 are known to have strong forbidden ion emission, the modeling also includes these lines, set to have the same width and shift as Fe II model. The list of [Fe II] lines is compiled from Véron-Cetty et al. (2004) (Table 3 in the Appendix). The model describes remarkably the observed spectrum, as seen through the residual spectrum (bottom panel, Fig. 7).

3.2.2. Sample of SDSS AGN spectra

We prepared the 655 spectra from the SDSS sample (through procedures listed in step 1) and subtracted the reconstructed host galaxy contribution (obtained through step 2) from the observed spectrum (see an example in Fig. 8). On the shown example, the host-galaxy contributes on the level of 76% to the observed continuum flux around 6000 Å. In a few cases when stellar contribution from the host galaxy is estimated to be below zero, it has not been subtracted from the observed spectrum. We then performed simultaneous multi-component spectral fitting with the `fantasy` code, aiming to measure the fluxes and widths of the pure broad component of Fe II, H γ , H β and H α lines.

We fitted the bulk of the spectra in the rest wavelength range $\sim 4000\text{--}7000\text{ \AA}$ using a single model¹⁰ consisting of: i) broken power-law continuum, to allow for the simultaneous fitting of the $H\alpha$ and $H\beta$ wavelength range, which could have a different continuum slope (Vanden Berk et al. 2001); the breaking point was set to be in the range $5350\text{--}5650\text{ \AA}$, which is free from strong emission lines; ii) broad hydrogen ($H\alpha$, $H\beta$, $H\gamma$, $H\delta$) and helium (He I 5877 \AA , He II 4686 \AA) lines; iii) very broad component for strong hydrogen lines ($H\alpha$, $H\beta$, $H\gamma$) lines; iv) standard strong narrow emission lines, all fixed to have the same shifts and widths as [O III] 5007 \AA : [O III] 4363 \AA , [O III] $\lambda\lambda 4959, 5007\text{ \AA}$, [N II] $\lambda\lambda 6548, 6583\text{ \AA}$, [S II] $\lambda\lambda 6716, 6731\text{ \AA}$, [O I] $\lambda\lambda 6300, 6364\text{ \AA}$; the ratios of [O III] and [N II] doublets were fixed to 3 (Dimitrijević et al. 2007; Kovačević-Dojčinović et al. 2022; Dojčinović et al. 2023); v) the broad component of the [O III] doublet, which line ratio is also fixed to 3, and have same width and shift (Kovačević-Dojčinović et al. 2022); vi) optical Fe II model, described in Section 3.1, in which all lines have same width and shift. The χ^2 was used to test for the goodness of the fitting results, however all results were also visually inspected.

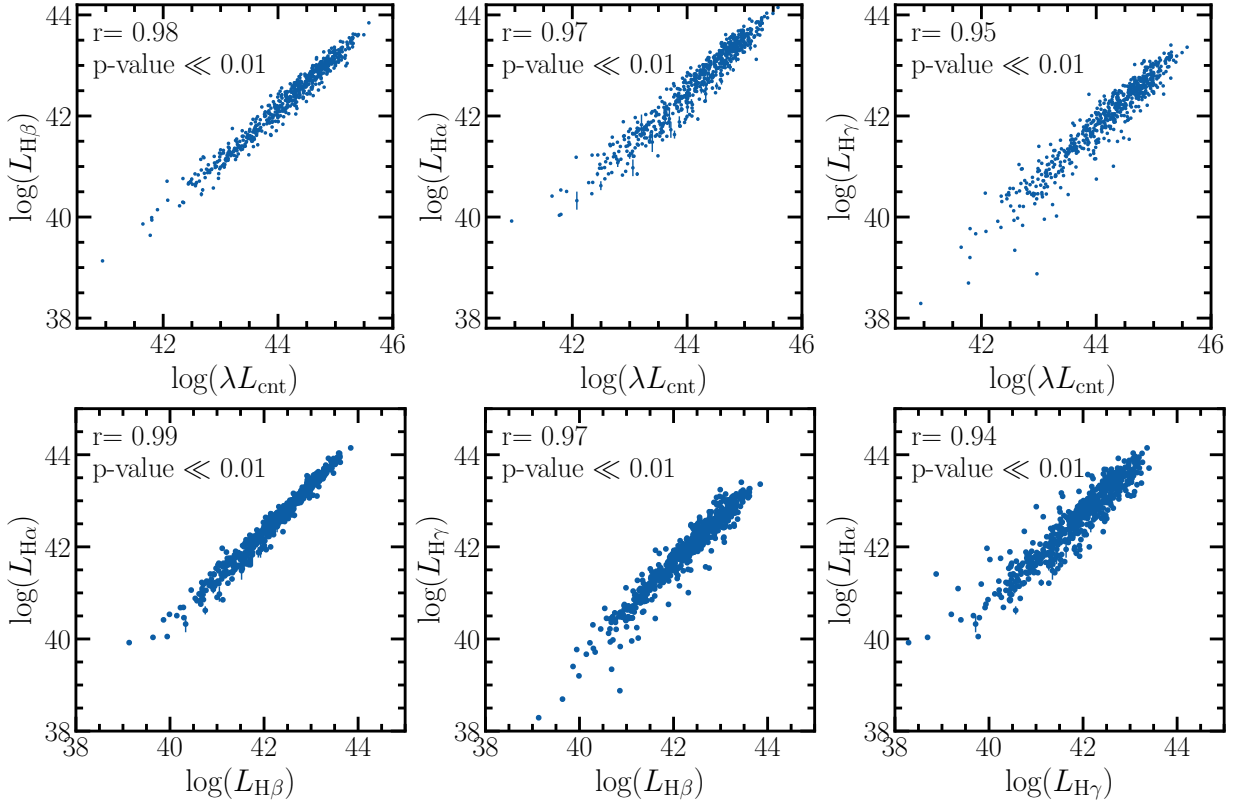


Figure 10. Luminosity (in erg s^{-1}) of the broad $H\alpha$ (left), $H\beta$ (middle), and $H\gamma$ (right) line as a function of the continuum luminosity $\lambda L_{\text{cont}}\text{ \AA}$ at 5100 \AA (upper panels) and for broad $H\alpha$ vs. $H\beta$ (left), $H\alpha$ vs. $H\gamma$ (middle), and $H\beta$ vs. $H\gamma$ (right) for the whole SDSS sample (bottom panels). Pearson correlation coefficient together with corresponding p-value is indicated on each plot.

4. RESULTS AND DISCUSSION

The sample of 655 SDSS spectra were fitted with the single spectral model defined in the previous section (a few examples are given in Fig. 9). After visual inspection, 34 objects ($\sim 5\%$) were excluded from further analysis, mostly due to lower S/N or very broad or double-peaked profiles, which could not be addressed with the single model described here. We have noticed that in a few cases, the underlying stellar continuum was well reproduced (based on the galaxy absorption features), and subtracted, however the pure AGN spectra were still showing a slight increase towards larger wavelength (as illustrated in the bottom panel of Figure 9). This continuum reddening could be interpreted either as

¹⁰ Fittings were run on the SUPERAST computer cluster of the Department of Astronomy, University of Belgrade - Faculty of Mathematics (Kovacevic et al. 2022).

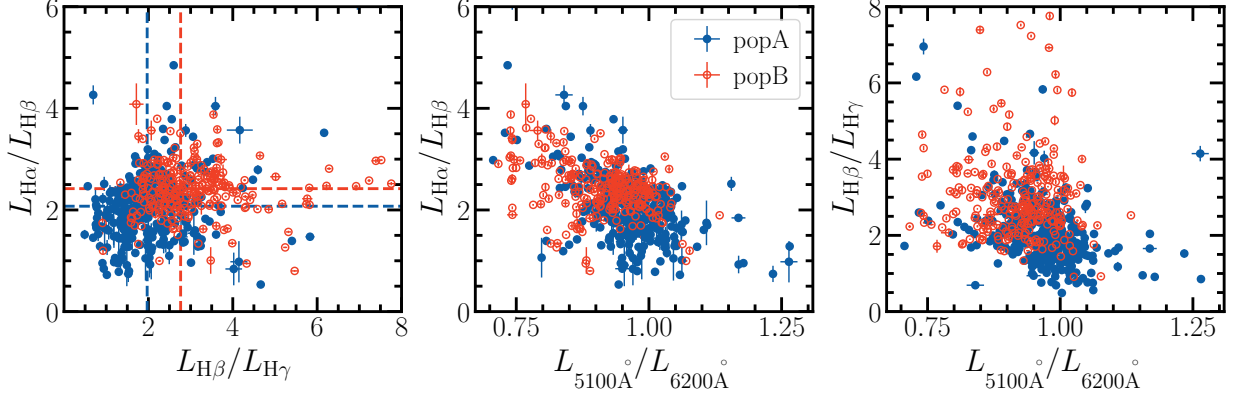


Figure 11. Balmer decrement $H\alpha/H\beta$ vs. $H\beta/H\gamma$ (left) for pop A (blue) and pop B (red) sub-samples. Middle and right panel show $H\alpha/H\beta$ and $H\beta/H\gamma$ vs. ratio continuum luminosities at 5100 Å and 6200 Å. Significant anti-correlation is seen with the continuum ratio: for pop A object $r = -0.51$ ($p_0 \ll 0.01$) for $H\alpha/H\beta$ and $r = -0.40$ ($p_0 \ll 0.01$) for $H\beta/H\gamma$, and for pop B object $r \sim -0.39$ ($p_0 \ll 0.01$) for $H\alpha/H\beta$ and $r = -0.25$ ($p_0 \ll 0.01$) for $H\beta/H\gamma$.

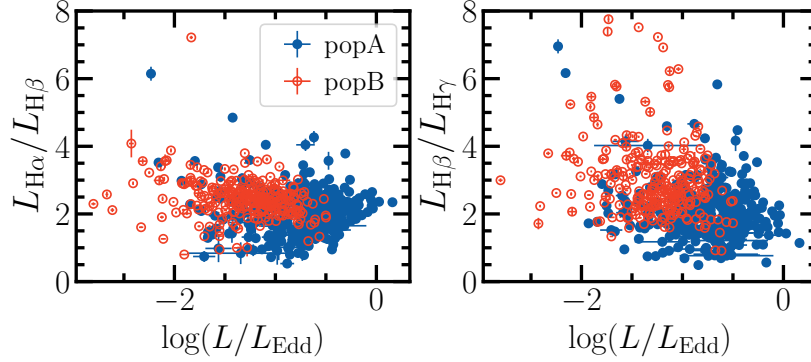


Figure 12. Balmer decrement $H\alpha/H\beta$ (left) and $H\beta/H\gamma$ (right) for pop A (blue) and pop B (red) sub-samples vs. Eddington ratio (L/L_{Edd}). Pearson correlation coefficients point to no correlations: for pop A object $r = 0.05$ ($p_0 = 0.3$) for $H\alpha/H\beta$ and $r = -0.22$ ($p_0 < 0.01$)

for $H\beta/H\gamma$, and for pop B object $r \sim -0.24$ ($p_0 < 0.01$) for $H\alpha/H\beta$ and $r \sim -0.16$ ($p_0 = 0.01$) for $H\beta/H\gamma$.

a result of poor removal of the host-galaxy stellar continuum using the method of spectral decomposition with galaxy templates, or possibly we see traces of the contribution coming from a tail-end of thermal emission from the hot dust present within the AGN.

After decomposing the spectra into individual components, we measured the following spectral parameters from the best-fit model: broad $H\alpha$, $H\beta$, and $H\delta$ fluxes, continuum luminosities (λL_λ) at 5100 Å and 6200 Å (median integral in 5090–5110 Å and 6190–6210 Å respectively, from the reconstructed pure AGN spectra, Figure 8), and Fe II in three different windows: Fe II blue (4340–4680 Å), Fe II green (5100–5600 Å), and Fe II red (6100–6650 Å). Fluxes were measured from the modeled broad line profiles and continuum, and then converted to luminosities based on the luminosity distance calculated from the cosmological redshift and adopted cosmological parameters (see Section 1). The Fe II blue band was used to get the R_{FeII} parameter. The FWHM of the lines is also measured, and in case of broad Hydrogen lines, which were fitted with two Gaussians, the width of the total broad line was calculated. From the measured continuum luminosity at 5100 Å and FWHM of $H\beta$ line, we get the M_{BH} through standard single-epoch method for SMBH mass estimates (see e.g., Popović 2020; Dalla Bontà et al. 2020). Once we have M_{BH} , the Eddington luminosity is simply $L_{\text{Edd}} = 1.26 \times 10^{38} (M_{\text{BH}}/M_\odot) \text{ erg s}^{-1}$. For the bolometric luminosity $L_{\text{bol}} = k_{\text{bol}} \lambda L_\lambda$ we used the mean quasar bolometric correction $k_{\text{bol}} \approx 10$ (e.g., Richards et al. 2006) and the continuum luminosity at 5100 Å. This then gives the Eddington ratio $L_{\text{Edd}}/L_{\text{bol}}$. The uncertainties of measured quantities are calculated as described in Section 3.2 (step 6), and then further propagated for derived quantities like luminosity or Eddington ratio. Some measured quantities, especially of strong broad emission lines (e.g. fluxes of $H\alpha$ and $H\beta$ lines or Fe II lines in the

sample of xA objects) have low uncertainties, which is a result of spectra being selected to have higher $S/N > 35$. For cases when we could not estimate the uncertainties, we used the mean value [in %] to get the uncertainty of the measured quantity.

Table 2 lists the measured spectral parameters with uncertainties, that is: the SDSS object ID, redshift, broken power-law indices of the fitted underlying AGN continuum (α_1, α_2 where α_1 describes the part of spectra with wavelengths larger than the break wavelength, and $\alpha_1 + \alpha_2$ the lower ones), continuum luminosity L_{5100} and L_{6200} , the $H\alpha$, $H\beta$ broad line luminosities, as well as the luminosities of Fe II blue, green, red, the full width half a maximum of the broad $H\alpha$, broad $H\beta$, and Fe II lines, and Eddington ratio L/L_{Edd} . The last row gives the mean average quantities for the total SDSS sample. Table 2 is available in its entirety in the machine-readable format in the online Journal.

4.1. Hydrogen Balmer lines

First we present our results for the hydrogen Balmer lines in the total sample. Figure 10 (upper panels) shows the strong correlation of the luminosity of broad Balmer lines ($H\alpha$, $H\beta$, $H\gamma$) as a function of the continuum luminosity L_{5100} , for the whole SDSS sample. High Pearson correlation coefficients close to unity support this. Strong correlations between line and continuum luminosities have been observed before by many studies in both single object (e.g., Ilić et al. 2017; Dalla Bontà et al. 2020) and larger samples (e.g., Liu et al. 2019; Rakshit et al. 2020), supporting that the results obtained through the *fantasy* fittings are in agreement with previous findings. The observed line-continuum correlations are expected if photoionization by the central continuum emission is the main heating source of the BLR and thus responsible for the broad line emission (Osterbrock & Ferland 2006; Netzer 2013). In case of $H\gamma$ line (Fig. 10, right panels), there is some scatter for lower line luminosities, probably due to difficulties to identify and subtract satellite lines such as [O III] $\lambda 4363$.

It is important to know that the intrinsic extinction due to the presence of dust within the AGN makes it unclear what fraction of luminosity is actually being measured (Kaspi et al. 2000). This AGN intrinsic reddening is still one of the critical points in the studies of the AGN phenomenon (Gaskell 2017). Dust is present not just in the host galaxy, but is also associated with the central regions of the AGN, and not just in the equatorial part typically explained by the unified model of AGN, but also in parsec-scale polar areas (Hönig et al. 2012; Stalevski et al. 2017). In this analysis we have performed only the correction for the host galaxy contribution, with which we assumed that the extinction within the galaxy (if present) has been removed. However, the effects of extinction within the AGN itself have not been assessed (as not in other studies, e.g. Calderone et al. 2017; Liu et al. 2019; Rakshit et al. 2020). Therefore, some contamination to the continuum luminosity may still exist due to intrinsic AGN extinction. The obtained strong luminosity correlations may point to the internal extinction being not strong in most type 1 AGN studied here, as pointed before by some authors (e.g., Calderone et al. 2017).

Strong correlations between different broad Balmer line luminosities ($H\alpha$ vs. $H\beta$, $H\alpha$ vs. $H\gamma$, and $H\beta$ vs. $H\gamma$) for the whole SDSS sample are also present (Figure 10, bottom panels). Especially in case of $H\alpha$ vs. $H\beta$ ($r=0.99$ for the total SDSS sample), implying that the emission lines have the same physical origin. This is supported with the same kinematics of these lines, as they have the same FWHM, as also shown in Rakić (2022). No difference is seen in above correlations when considering different populations, i.e. for pop A, pop B and xA sub-samples.

Table 2. Measured spectral quantities for the first 10 objects of the total SDSS sample. The last row gives the mean average quantities for the total SDSS sample.

SDSS Object ID	redshift	α_1, α_2	$\log \lambda L_{5100}$ erg/s	$\log \lambda L_{6200}$ erg/s	$\log L(H\beta)$ erg/s	$\log L(H\alpha)$ erg/s	$\log L(\text{Fe II}_{\text{blue}})$ erg/s	$\log L(\text{Fe II}_{\text{green}})$ erg/s	$\log L(\text{Fe II}_{\text{red}})$ erg/s	$w(H\beta)$ km/s	$w(H\alpha)$ km/s	$w(\text{Fe II})$ km/s	L/L_{Edd}
SDSS J145824.46 +363119.5	0.246	-2.31, -0.22	44.580±0.001	44.571±0.001	42.558±0.006	42.717±0.004	42.607±0.005	42.428±0.009	41.508±0.038	2829±35	4556±69	2378±25	0.283±0.008
SDSS J095302.64 +380145.2	0.273	-1.32, -1.04	44.609±0.001	44.637±0.001	42.888±0.003	43.289±0.001	42.407±0.020	42.253±0.012	42.059±0.018	3177±35	3037±23	3367±48	0.232±0.005
SDSS J225603.37 +273209.5	0.363	-2.11, -1.43	45.273±0.001	45.266±0.001	43.443±0.005	43.808±0.001	43.172±0.008	42.988±0.006	42.578±0.018	2900±69	2693±35	3451±50	0.580±0.030
SDSS J224113.54 -012108.8	0.058	-1.19, 0.94	43.135±0.002	43.196±0.001	41.384±0.003	41.756±0.002	40.650±0.046	40.007±0.104	40.256±0.045	6835±68	5729±1	2405±118	0.010±0.001
SDSS J105007.75 +113228.6	0.134	-2.03, -1.63	44.571±0.001	44.566±0.001	42.715±0.002	42.971±0.003	42.332±0.066	42.320±0.008	41.712±0.019	2209±35	2278±0	1963±32	0.459±0.015
SDSS J125851.45 +235526.6	0.075	0.56, -0.15	43.094±0.001	43.187±0.001	41.163±0.006	41.369±0.004	40.749±0.088	40.305±0.041	37.785±1.350	9661±242	6007±40	1945±129	0.005±0.000
SDSS J080131.96 +473616.0	0.157	-1.83, -0.84	44.691±0.001	44.695±0.001	42.886±0.011	43.310±0.002	42.514±0.016	42.246±0.007	42.046±0.013	7316±203	6494±69	6000±5	0.048±0.003
SDSS J125741.05 +202347.8	0.081	-1.38, -1.62	43.150±0.002	43.165±0.001	41.366±0.008	41.534±0.005	41.409±0.012	41.229±0.011	40.401±0.061	1450±35	1105±34	3575±251	0.221±0.010
SDSS J004719.39 +144212.6	0.039	-0.50, -1.19	43.178±0.001	43.235±0.001	41.215±0.004	41.634±0.002	40.895±0.010	40.253±0.035	40.341±0.038	2623±34	2485±14	2630±31	0.070±0.002
SDSS J154348.62 +401324.8	0.318	-1.55, -0.44	44.830±0.002	44.855±0.001	43.123±0.004	43.534±0.003	42.568±0.018	42.379±0.036	42.428±0.019	4831±69	4627±40	5419±158	0.128±0.004
Averaged		-1.42, -0.72	44.160±0.001	44.187±0.001	42.312±0.006	42.644±0.010	41.944±0.037	41.832±0.023	41.400±0.124	4132±78	3765±71	3218±132	0.164±0.011

NOTE—Columns give the SDSS object ID, redshift, indices α_1, α_2 of the broken power-law fitting the underlying AGN continuum, logarithm of the continuum luminosities at 5100 Å and 6200 Å (λL_λ), logarithm of the $H\beta$ and $H\alpha$ broad-line luminosities ($L(H\beta)$, $L(H\alpha)$), and luminosities of Fe II blue, green, red ($L(\text{Fe II}_{\text{blue}})$, $L(\text{Fe II}_{\text{green}})$, $L(\text{Fe II}_{\text{red}})$), the full width half maximum of the broad $H\beta$, broad $H\alpha$, and Fe II lines in km/s ($w(H\beta)$, $w(H\alpha)$, $w(\text{Fe II})$), and the Eddington ratio L/L_{Edd} . Table 2 is published in its entirety in the machine-readable format. A portion is shown here for guidance regarding its form and content.

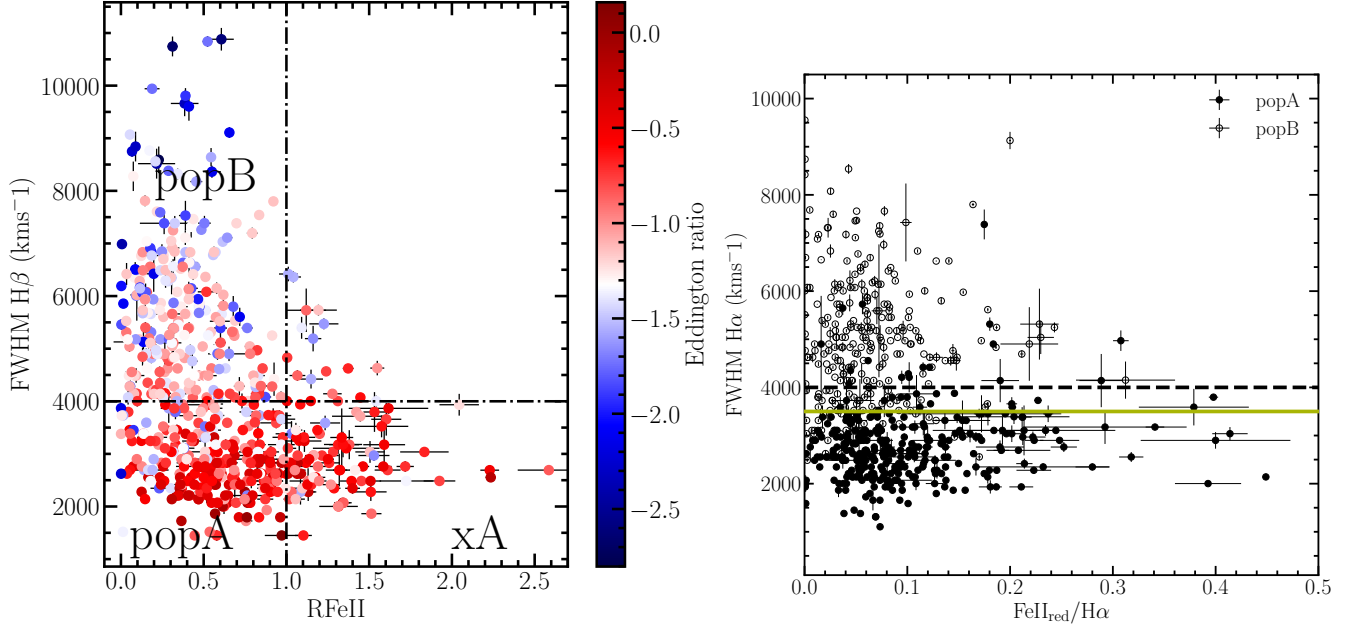


Figure 13. *Upper:* SDSS sample plotted on the main sequence diagram (FWHM($H\beta$) vs. R_{FeII}). Horizontal (FWHM($H\beta$)=4000 km s^{-1}) and vertical ($R_{\text{FeII}}=1$) line divide the population B (pop B), population A (pop A), and extreme population A (xA). Eddington ratio (L/L_{Edd}) is shown on the colorbar. *Bottom:* Same diagram produced using the $H\alpha$ FWHM and Fe II red (6100–6650 \AA) emission. Pop A and B identified through the upper main sequence are marked with different symbols. Dashed and solid lines mark the position of FWHM($H\alpha$)=4000 km s^{-1} and FWHM($H\alpha$)=3500 km s^{-1} , respectively.

The ratio of Balmer lines can tell us about the physical processes of the region where they originate from (e.g., La Mura et al. 2007; Ilić et al. 2012). Balmer decrement $H\alpha/H\beta$ vs. $H\beta/H\gamma$ is given in Figure 11, in which Pop A and Pop B objects occupy slightly different areas. Pop B show higher Balmer decrement (average $H\alpha/H\beta=2.42$, $H\beta/H\gamma=2.76$) than pop A objects (average $H\alpha/H\beta=2.07$, $H\beta/H\gamma=1.97$). These values are below those ($H\alpha/H\beta \approx 3$) suggested by pure recombination theory. One possibility could be that collisional deexcitation is decreasing the $H\alpha$ line, and thus giving a lower $H\alpha/H\beta$ ratio. It is noteworthy that in our results $H\alpha$ flux may be systematically lower, since a part of the emission is allocated to Fe II lines.

The relationship between the Balmer decrement and the ratio of continuum measured at 5100 \AA and 6200 \AA can be seen in Fig. 11. A significant low-level anti-correlation is somewhat stronger for pop A object ($r = -0.51$ ($p_0 \ll 0.01$) for $H\alpha/H\beta$, $r = -0.40$ ($p_0 \ll 0.01$) for $H\beta/H\gamma$) than in pop B object ($r \sim -0.39$ ($p_0 \ll 0.01$) for $H\alpha/H\beta$, $r = -0.25$ ($p_0 \ll 0.01$) for $H\beta/H\gamma$). As the continuum 5100/6200 ratio decreases, meaning the object becomes redder, the Balmer decrement increases. This suggests that the increase of the broad $H\alpha/H\beta$ ratio may be due to the low-level of reddening, at least in some fraction of object. On the other hand, the values of the Balmer decrement of broad lines $H\alpha/H\beta$ measured here are below the theoretical predictions in most objects (Calderone et al. 2017; Lu et al. 2019), making it hardly possible to assess extinction using $H\alpha/H\beta$ ratio. The possibility that this may however point to some dust presence is supported by previous studies showing that objects classified as “pop B” are more affected by dust due to their larger inclination angles, while “pop A” objects are seen more face-on and have lower inclination angles (Marziani et al. 2022), making them less affected by dust. We also demonstrate that Balmer decrement is not dependent on the Eddington ratio (L/L_{Edd}), as shown in Figure 12, supported with no correlation present (correlation coefficients $r \sim 0$). This is in agreement with the previous findings of Lu et al. (2019).

When plotted on the main sequence diagram (FWHM($H\beta$) vs. R_{FeII} , Fig. 13, upper panel), the SDSS sample occupies the expected parameter space (Marziani et al. 2018b). Moreover, the Eddington ratio (L/L_{Edd}) gradually rises from pop B to pop A sources (colorbar in Fig. 13), as expected (Du et al. 2016). The average values of L/L_{Edd} are 0.07, 0.24 and 0.23 for pop B, pop A, and xA samples, respectively. The dependence of the R_{FeII} sequence on the Eddington ratio has been also described through modeling with photoionization codes (Panda et al. 2019). Measuring the Fe II emission near the $H\alpha$ line, allowed us to construct for the first time a main sequence diagram using $H\alpha$ line and fluxes Fe II red (6100–6650 \AA), presented in Fig. 13, bottom panel). The same trend with the Eddington ratio

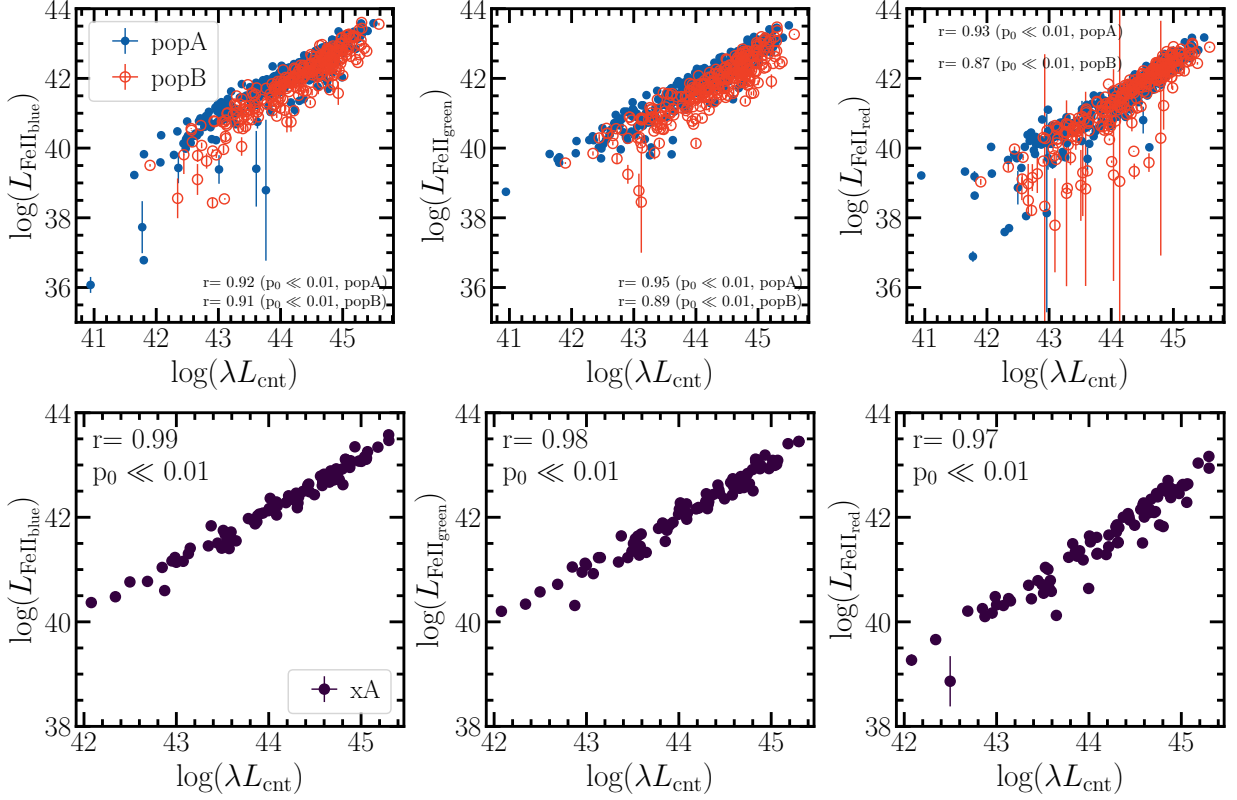


Figure 14. Upper panels show luminosity of Fe II in three bands (Fe II blue (left), Fe II green (middle), and Fe II red (right)) as a function of the continuum luminosity $L_{5100\text{\AA}}$ (given in erg s^{-1}) for the pop A (full circles) and pop B (open circles) samples. Bottom panels shows only a sub-sample of xA objects. Pearson correlation coefficient together with corresponding p-value is indicated on each plot.

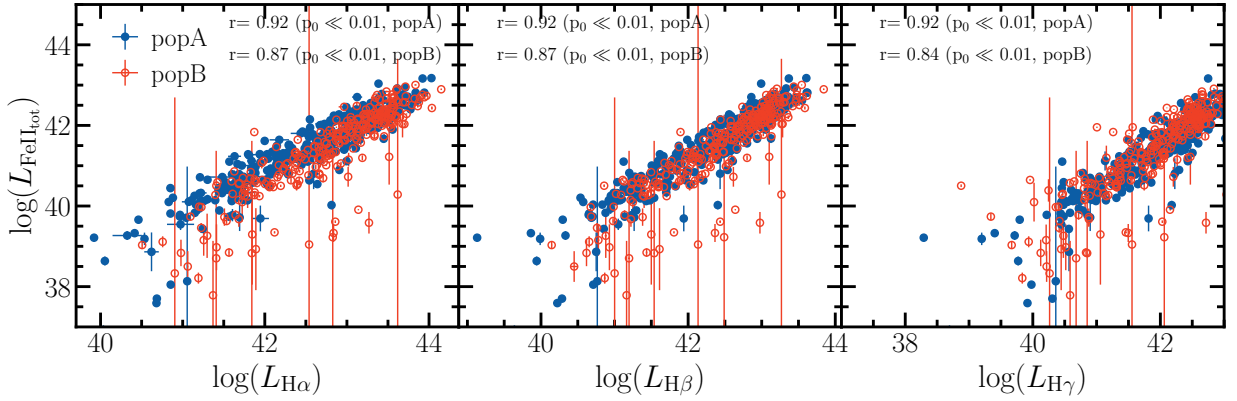


Figure 15. Total Fe II emission in pop A (full blue circles) and pop B (open red circles) samples with respect to the $\text{H}\alpha$ (left) and $\text{H}\beta$ (right) luminosities, in units erg s^{-1} . Pearson correlation coefficient together with corresponding p-value is indicated on each plot.

increasing from pop B toward pop A objects is also detected. Different populations identified through the standard main sequence diagram (Fig. 13, upper panel) occupy similar areas of $\text{H}\alpha$ widths and iron strength, only that Fe II (red) emission is much weaker than $\text{H}\alpha$ line. We note that the main sequence diagram for $\text{H}\alpha$ line points that the division line between pop A and pop B objects may be lower ($\text{FWHM}(\text{H}\alpha) \sim 3500 \text{ km s}^{-1}$), as indicated with a solid horizontal line in Fig 13, bottom panel.

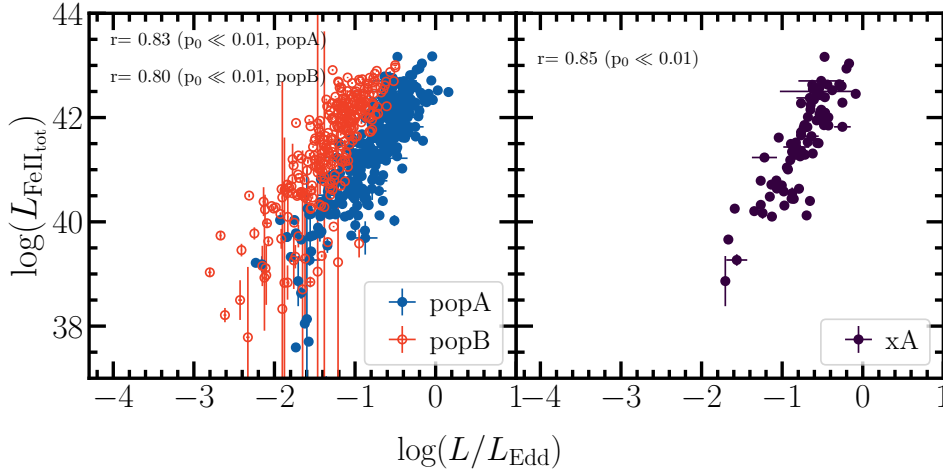


Figure 16. Total Fe II emission in pop A and pop B sample (left), and for xA sample (right) with respect to the Eddington ratio $L_{\text{Edd}}/L_{\text{bol}}$.

4.2. Fe II emission near $H\alpha$ and $H\beta$ wavelength bands

More compelling is to explore the behaviour of Fe II emission with respect to other spectral features. Here we study total Fe II emission and in three selected wavelength bands (Fe II blue 4340–4680 Å, Fe II green 5100–5600 Å, and Fe II red 6100–6650 Å) in three populations of type 1 AGN, i.e. in pop A, pop B and xA sub-samples.

In Figure 14 (upper panels), we plot the luminosity of Fe II in three bands: Fe II blue (left), Fe II green (middle), and Fe II red (right) as a function of the continuum luminosity $L_{5100\text{Å}}$ for the pop A (full circles) and pop B (open circles) samples. Significant correlation is seen for all three studied iron bands, pointing to the importance of the central continuum emission for the Fe II line production. It seems the scatter is slightly larger for pop B objects, however significant correlation is present for both sub-samples (correlation coefficient indicated in Figure 14, upper panels). Similar trends have been observed before by Dong et al. (2011), but they report a lower level of correlations and larger scatter probably due to much lower quality of the studied sample. We note that in case of objects with weaker Fe II emission (or spectra of low S/N), it is more difficult to detect Fe II lines as they blend with the continuum. This is probably the reason behind the scatter seen in Fe II (red) emission in pop B objects (see right panels in Fig. 14). In case of xA sample, the correlation with the continuum luminosity is even stronger for all three iron bands (Fig. 14, bottom panels).

Detailed studies of the Fe II emission, including modeling and observations point to complex excitation mechanisms involved in its production. In their theoretical calculations of Fe II emission, Sigut & Pradhan (2003) used for the excitation mechanisms: continuum and line ($\text{Ly}\alpha$, $\text{Ly}\beta$) fluorescence, collisional excitation, and self-fluorescence among the Fe II transitions. Some other studies show that collisional excitation is an important driver of the Fe II optical emission, with $\text{Ly}\alpha$ fluorescence contributing on the level of $\sim 20\%$ (Baldwin et al. 2004; Garcia-Rissmann et al. 2012; Marinello et al. 2016). Some evidence for photoionization by the central source as responsible for the Fe II emission comes from variability studies. For example, Barth et al. (2013) showed that Fe II emission in two Seyfert 1 galaxies, NGC 4593 and Mrk 1511, does reverberate on short timescales in response to continuum variations, pointing to the origin of the Fe II emission in photoionized gas in the BLR. Shapovalova et al. (2012) found that in a NLSy1 Ark 564, there is a slightly better correlation of optical Fe II with the continuum at 5100 Å than in the hydrogen Balmer lines, whereas in the case of another NLSy 1 galaxy NGC 4051, the variability of the optical Fe II emission also follows the continuum variability (Wang et al. 2005). However, in other two cases, NGC 5548 (Vestergaard & Peterson 2005) and Ark 120 (Kuehn et al. 2008), weak correlation is seen, which might be due to poor cadence of the monitoring data, despite the large length of monitoring campaigns. Our findings may support the assumption that the central continuum emission is governing the production of Fe II lines (Gaskell et al. 2022). Based on the strong correlations between the Balmer lines and continuum luminosities, assuming that the continuum luminosity at 5100 Å is a good tracer of ionization continuum, it is reasonable to assume that the $\text{Ly}\alpha$ line could correlate with the continuum luminosity at 5100 Å. Therefore, we cannot rule out the possibility that continuum and $\text{Ly}\alpha$ -pumping may be responsible for the excitation of Fe II upper levels (considering that this line is broad enough), which then

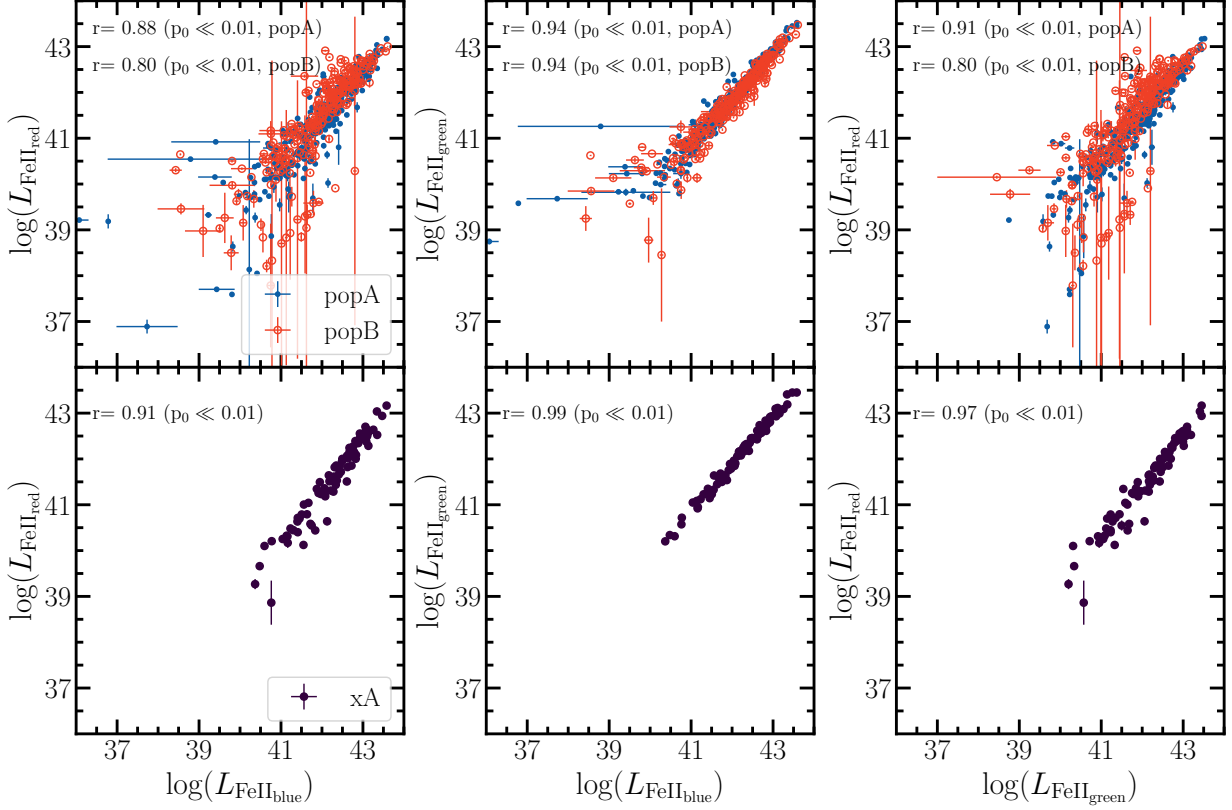


Figure 17. Correlations between luminosity of Fe II in three bands: Fe II blue (4340–4680 Å), Fe II green (5100–5600 Å), and Fe II red (6100–6650 Å) for the pop A (blue circles) and pop B (red circles) samples (upper panels), and only for the population of extreme A objects (bottom panels). Pearson correlation coefficient together with corresponding p-value is indicated on each plot.

populate the upper levels of transitions leading to optical Fe II. As already stated, some previous work emphasized the importance of Ly α fluorescence in Fe II production in AGN (e.g., Penston 1987; Sigut & Pradhan 1998, 2003; Sarkar et al. 2021). Some authors claimed that in NLSy1 other mechanisms, such as collisional excitation could be contributing as well to the Fe II production (e.g., Collin & Joly 2000). However, here we see no difference in pop A and xA samples (which could be considered as representatives of NLSy1 objects) but even stronger dependence on the continuum luminosity. This is supported with strong correlations between the total Fe II emission with respect to the H α and H β luminosities in both populations (Fig. 15). Photoionization by the accretion disc continuum is also indicated by the correlation of Fe II emission with the accretion rate. Figure 16 shows total Fe II emission in pop A and pop B sample (left), and for xA sample (right) with respect to the Eddington ratio $L_{\text{Edd}}/L_{\text{bol}}$. A clear division between pop A and pop B objects is seen, where pop A objects have stronger Eddington ratio. A strong correlation of Fe II emission in the optical band with $L_{\text{Edd}}/L_{\text{bol}}$ is seen, which has been reported before (Dong et al. 2011). Since the heating of the BLR plasma is dominantly through photoionization (Osterbrock & Ferland 2006), this implies that the rate of collisions could be directly proportional to the input continuum ionizations. Therefore, with our findings we cannot rule out the effects of photoionization on the Fe II emission, influencing through all excitation mechanisms, i.e., collisional excitation, continuum and Ly α fluorescence. We believe that simultaneous observations of Fe II emission in AGN from UV to NIR are needed to understand the connection between these different physical processes and different Fe II emission.

Iron emission measured in three different wavelength bands, i.e. Fe II blue, Fe II green, and Fe II red is present in all objects, with Fe II (red) being somewhat weaker (Fig. 14, right panels). Pop B sample also contains objects with the strongest Fe II emission (red circled, Fig. 17, upper panels). This is not typically assumed, as strong Fe II emission is usually attributed to pop A (and NLSy1 as their subset). This could be the result of the fact that in these objects Fe II lines are broader and blended with underlying continuum or hidden in broad H α wings, and thus difficult to extract

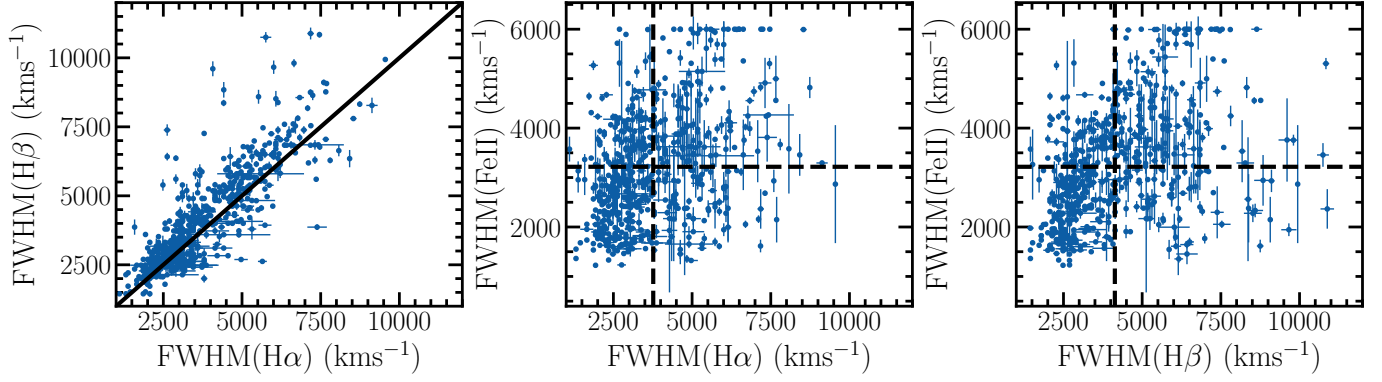


Figure 18. Width of the broad H β plotted against the width of broad H α line (left) for the total SDSS sample, as well as the width of Fe II emission versus H α (middle) and H β (right) broad line width. Line widths are in units of km s $^{-1}$. Linear best-fitting line is displayed in H β vs. H α plot, whereas on the two plots dashed lines denote the average values for the total sample.

(see examples in Fig. 9). This is why simultaneous multi-component fitting of AGN spectra, which is the approach implemented in *fantasy* code, may be important in studying the Fe II emission.

The most relevant finding of this analysis is the strong correlation between luminosity of Fe II in three bands (blue, green, red) for pop A and pop B samples (Fig. 17, upper panels). The strongest correlation is seen between the blue and green Fe II band ($r=0.94$ in pop A and pop B) which is expected since these bands are populated with most Fe II transitions (Figs. 2 and 5). These two bands surrounding H β line are the ones typically measured and most Fe II templates are tackling these Fe II emission (Boroson & Green 1992; Véron-Cetty et al. 2004; Tsuzuki et al. 2006; Park et al. 2022). However, the Fe II emission in the red band, redward from H α line, is also present and correlates with the iron emission present in the vicinity of H β line (Fig. 17, left and right panels). When only xA sample is considered (Fig. 17, bottom panels), the correlations between Fe II bands are even stronger.

Therefore, the red Fe II emission is contaminating the blue wing of H α , whereas the red wing is significantly less affected (Fig. 9). These iron blends are somewhat weaker and maybe hidden in the underlying continuum emission and broad H α wings in pop B objects (with broader emission lines), especially in low-quality spectra (i.e., poor S/N and spectral resolution). Some authors have been attributing this emission to broad line wings of H α line, for which an additional very broad line component had to be introduced (as e.g., in Calderone et al. 2017). This may significantly influence the measurements of H α flux and width, and their consequent application. For example, presence of Fe II emission could be responsible for the scatter of M_{BH} when measured from H α line (Greene & Ho 2005; Dalla Bontà et al. 2020).

Finally, we check the kinematics of Fe II lines with respect to the broad H α and H β lines through the analysis of the line FWHM. Figure 18 presents the width of Fe II emission versus H α (middle) and H β (right) broad line width for the total SDSS sample. The average width of Fe II lines in total sample is ~ 3300 km s $^{-1}$, whereas H α FWHM is ~ 3780 km s $^{-1}$ and H β is ~ 4120 km s $^{-1}$. The two broad components used to fit the H α line have the widths of 6640 km s $^{-1}$ (6300 km s $^{-1}$ for H β) and 2470 km s $^{-1}$ (2450 km s $^{-1}$ for H β). This is in agreement with the previous assumption that Fe II emission is originating in so called intermediate line region (Kovačević et al. 2010; Dong et al. 2011).

4.3. Fittings of type 1 AGN spectra with *fantasy* code

Using the *fantasy* code, we successfully modeled the AGN optical spectra ($\lambda\lambda$ 4000-7000 Å) by fitting all emission components simultaneously: the underlying broken power-law continuum, broad and narrow emission lines, and the Fe II model (Fig. 9). The observed strong correlations between the line and continuum luminosities, and between the broad line luminosities indicate good performance of the automatic spectral fitting with the *fantasy* code. This is also confirmed by the strong correlation between the FWHMs of H α and H β line (Fig. 18, left panel). We note that in few cases ($< 3\%$) the width of Fe II lines was pegged to the upper limit set by the code (Fig. 18, middle and right panels). These objects are pop B with very strong Fe II emission in all three bands. We visually inspected these fits, and found that the broad H α and H β , and Fe II bands were well fitted, from which we concluded that line fluxes have been correctly extracted. These could generally be removed from the analysis, or fitted with models that have lower

constraints on the limits, but, for consistency, we decided to include them, as they are not influencing the presented results.

In addition, we have shown that especially when investigating the $H\alpha$ line, the use of the `fantasy` code can be important to detect the Fe II emission hidden in the $H\alpha$ wings and to carefully measure its spectral parameters. Overall, our findings show that the `fantasy` code is well suited for modeling SDSS type 1 AGN spectra. Finally, we have demonstrated that even in case of strong iron emitters, such as I Zw 1, the fittings using all emission components reproduced well the observed spectrum, especially in the vicinity of $H\alpha$ line (Fig. 7).

In addition to other well specialized program packages for AGN spectral fittings, namely `pyQSOFit` (Guo et al. 2018, 2019) and `QSfit` (Calderone et al. 2017), which are widely used in analysis of SDSS data (see e.g., Shen et al. 2011, 2019; Rakshit et al. 2020), the `fantasy` code seems to be also well suited to decompose the continuum and various emission features in AGN spectra. Its useful features are that it is user-friendly, contains necessary procedures for pre-processing and preparing the spectra for spectral decomposition, and the approach to simultaneously fit the emission lines and underlying continuum. In addition, the predefined lists of possible emission lines in AGN (e.g. strong narrow lines, see Table 3 in the Appendix), models with emission lines with fixed parameters (width, shift, line ratios), and model of Fe II emission, make `fantasy` a unique tool. However, apart from a numerical estimate of uncertainties from the fittings using the Monte Carlo approach, `fantasy` lacks a more serious treatment of uncertainties, which should be addressed in the future.

Nevertheless, the features listed above (e.g., simultaneous fitting of different components, predefined line lists, flexibility to model a wide variety of spectra) make this code well suited for modeling optical AGN spectra. Of particular interest are the modeling of optical spectra in transient events, such as the strong iron TDEs, which was shown to be successful by Petrushevska et al. (2023).

5. SUMMARY

We present here the study of the physical properties of broad line emitting regions in type 1 AGN, with special attention to Fe II emission in the wavelength range of the $H\alpha$ line. We use a sample of 655 objects from the current SDSS DR17, selected to cover the wavelength range 4000-7000 Å (i.e., containing both $H\alpha$ and $H\beta$ lines). Our goal is to analyze only high-quality spectra (S/N ratio >35) so that we can reliably measure Fe II emission around $H\beta$ but also near the $H\alpha$ line, where it is typically blended with underlying continuum and broad $H\alpha$ wings, particularly in low S/N spectra. We present an updated approach to multicomponent fitting of AGN spectra using the Python code `fantasy`. We present an extended model of Fe II emission based only on the atomic data, covering the wavelength range near the $H\alpha$ line, which has been poorly studied in the past. We perform spectral fitting using the code `fantasy`, which allowed us to measure the spectral parameters of the broad $H\gamma$, $H\beta$ and $H\alpha$ lines from the pure AGN spectra, as well as the iron emission in three bands: Fe II blue (4340–4680 Å), Fe II green (5100–5600 Å), and Fe II red (6100–6650 Å).

Our main conclusions can be summarized as follows:

1. The Fe II emission, if present in the vicinity of $H\beta$ line, is also detected redward from $H\alpha$ line, at a comparable strength. This red Fe II emission contaminates the broad $H\alpha$ line red-wing, which can have an impact on the measured $H\alpha$ flux and width. This can be particularly important for pop B objects (with broader emission lines), since iron blends near the $H\alpha$ line are hidden in the underlying continuum and broad $H\alpha$ wings;
2. The production of Fe II emission is strongly correlated with Eddington luminosity, and appears to be controlled by the same mechanism as the hydrogen Balmer lines, as shown by strong correlations with continuum and line luminosities. This implies that photionization is governing the Fe II production, however the exact mechanism (e.g., collisional excitation, continuum or $Ly\alpha$ fluorescence) is not constrained through this analysis;
3. Simultaneous multicomponent fitting of complex AGN spectra is a necessary approach for broad line parameter extraction, especially for reliable measurement of $H\alpha$ spectral parameters (width and flux). The open-source code `fantasy` tested in this work appears to be well suited for modeling the spectrum of type 1 AGN and may prove useful in future studies of a large number of AGN spectra.

To date, most Fe II templates have focused on the $H\beta$ line, which is one of the best studied AGN emission lines. However, with current and future high-precision instruments that will focus more on the NIR spectrum, observation

of the H α line in distant quasars will be more present, and more Fe II templates and models in this wavelength range will be needed.

Authors would like to thank the anonymous referee whose comments and suggestions helped to improve this manuscript. D.I. and L.Č.P. acknowledge funding provided by the University of Belgrade - Faculty of Mathematics (the contract №451-03-47/2023-01/200104) and Astronomical Observatory Belgrade (the contract №451-03-47/2023-01/200002) through the grants by the Ministry of Science, Technological Development and Innovation of the Republic of Serbia. D.I. acknowledges the support of the Alexander von Humboldt Foundation.

This research uses data from the SDSS Data Release 17 (Abdurro'uf et al. 2022). Funding for the Sloan Digital Sky Survey IV has been provided by the Alfred P. Sloan Foundation, the U.S. Department of Energy Office of Science, and the Participating Institutions. SDSS-IV acknowledges support and resources from the Center for High Performance Computing at the University of Utah. The SDSS website is www.sdss4.org.

This research has made use of the NASA/IPAC Extragalactic Database (NED), which is operated by the Jet Propulsion Laboratory, California Institute of Technology, under contract with the National Aeronautics and Space Administration.

Facilities: SDSS (Abdurro'uf et al. 2022), NED, NIST (Kramida et al. 2022), SUPERAST (Kovacevic et al. 2022).

Software: astropy (Astropy Collaboration et al. 2013, 2018), sherpa (Burke et al. 2022), fantasy (Ilić et al. 2020; Rakić 2022), sfdmap (Schlegel et al. 1998), PyAstronomy (Czesla et al. 2019), spectres (Carnall 2017).

APPENDIX

A. FANTASY PREDEFINED LINE LISTS

We provide all predefined lists of standard AGN emission lines present in the `fantasy` code. These are: Hydrogen lines (Balmer and Paschen series), Helium lines (both He I and He II), strongest narrow emission lines ([O III], [N II]), other AGN narrow lines (e.g., [S II], [O I]), other AGN broad lines (Ca I, O I), coronal lines (e.g. [Fe X], [Ar V]), and forbidden Fe II lines (Table 3). The presented list is very extensive, and most of the lines are not detected in AGN (see e.g., mean quasar spectrum from Vanden Berk et al. 2006). However, we believe that such a comprehensive single list of possible emission lines is useful.

When constructing these line lists (Table 3) we acknowledge the usage of a collection of detected emission lines in galaxies compiled by S. Drew Chojnowski¹¹, the NIST database (Kramida et al. 2022), narrow lines listed in Véron-Cetty et al. (2004) and Park et al. (2022), some of the solar coronal lines (Del Zanna & DeLuca 2018), as well as other papers cited in Section 3.

For all listed lines, we provide the air wavelengths. Full data sets are also available in the machine readable format.

¹¹ <http://astronomy.nmsu.edu/drewski/tableofemissionlines.html>

Table 3. Predefined lists of emission lines used in **fantasy** code.

Line	Wavelength (air)	Type	Group
Å			
H ϵ	3970.08	narrow, broad	hydrogen
H δ	4101.74	narrow, broad	hydrogen
H γ	4340.47	narrow, broad	hydrogen
H β	4861.33	narrow, broad	hydrogen
H α	6562.82	narrow, broad	hydrogen
Pa14	8598.39	narrow, broad	hydrogen
Pa13	8665.02	narrow, broad	hydrogen
Pa12	8750.47	narrow, broad	hydrogen
Pa11	8862.78	narrow, broad	hydrogen
Pa10	9014.91	narrow, broad	hydrogen
Pa9	9229.01	narrow, broad	hydrogen
Pa ϵ	9545.97	narrow, broad	hydrogen
Pa δ	10049.37	narrow, broad	hydrogen
Pa γ	10938.09	narrow, broad	hydrogen
...

NOTE—Columns give line wavelength in air (in Å), a type of line in terms of line width expected in AGN spectra, and a group assigned within a predefined list in **fantasy** code. Table 3 is published in its entirety in the machine-readable format. A portion is shown here for guidance regarding its form and content.

REFERENCES

- Abdurro'uf, Accetta, K., Aerts, C., et al. 2022, *ApJS*, 259, 35, doi: [10.3847/1538-4365/ac4414](https://doi.org/10.3847/1538-4365/ac4414)
- Ahumada, R., Prieto, C. A., Almeida, A., et al. 2020, *ApJS*, 249, 3, doi: [10.3847/1538-4365/ab929e](https://doi.org/10.3847/1538-4365/ab929e)
- Astropy Collaboration, Robitaille, T. P., Tollerud, E. J., et al. 2013, *A&A*, 558, A33, doi: [10.1051/0004-6361/201322068](https://doi.org/10.1051/0004-6361/201322068)
- Astropy Collaboration, Price-Whelan, A. M., Sipőcz, B. M., et al. 2018, *AJ*, 156, 123, doi: [10.3847/1538-3881/aabc4f](https://doi.org/10.3847/1538-3881/aabc4f)
- Baldwin, J. A., Ferland, G. J., Korista, K. T., Hamann, F., & LaCluyzé, A. 2004, *ApJ*, 615, 610, doi: [10.1086/424683](https://doi.org/10.1086/424683)
- Baron, D., Stern, J., Poznanski, D., & Netzer, H. 2016, *ApJ*, 832, 8, doi: [10.3847/0004-637X/832/1/8](https://doi.org/10.3847/0004-637X/832/1/8)
- Barth, A. J., Pancoast, A., Bennert, V. N., et al. 2013, *ApJ*, 769, 128, doi: [10.1088/0004-637X/769/2/128](https://doi.org/10.1088/0004-637X/769/2/128)
- Bellm, E. C., Kulkarni, S. R., Barlow, T., et al. 2019, *PASP*, 131, 068003, doi: [10.1088/1538-3873/ab0c2a](https://doi.org/10.1088/1538-3873/ab0c2a)
- Boroson, T. A., & Green, R. F. 1992, *ApJS*, 80, 109, doi: [10.1086/191661](https://doi.org/10.1086/191661)
- Bruhweiler, F., & Verner, E. 2008, *ApJ*, 675, 83, doi: [10.1086/525557](https://doi.org/10.1086/525557)
- Burke, D., Laurino, O., wmlaugh, et al. 2022, *sherpa/sherpa*: Sherpa 4.15.0, 4.15.0, Zenodo, doi: [10.5281/zenodo.7186379](https://doi.org/10.5281/zenodo.7186379)
- Calderone, G., Nicastro, L., Ghisellini, G., et al. 2017, *MNRAS*, 472, 4051, doi: [10.1093/mnras/stx2239](https://doi.org/10.1093/mnras/stx2239)
- Carnall, A. C. 2017, arXiv e-prints, arXiv:1705.05165, doi: [10.48550/arXiv.1705.05165](https://doi.org/10.48550/arXiv.1705.05165)
- Chelouche, D., Pozo Nuñez, F., & Kaspi, S. 2019, *Nature Astronomy*, 3, 251, doi: [10.1038/s41550-018-0659-x](https://doi.org/10.1038/s41550-018-0659-x)
- Collin, S., & Joly, M. 2000, *NewAR*, 44, 531, doi: [10.1016/S1387-6473\(00\)00093-2](https://doi.org/10.1016/S1387-6473(00)00093-2)
- Czerny, B., Zajaček, M., Naddaf, M.-H., et al. 2022, arXiv e-prints, arXiv:2211.11022, doi: [10.48550/arXiv.2211.11022](https://doi.org/10.48550/arXiv.2211.11022)
- Czesla, S., Schröter, S., Schneider, C. P., et al. 2019, *PyA*: Python astronomy-related packages. <http://ascl.net/1906.010>
- Dalla Bontà, E., Peterson, B. M., Bentz, M. C., et al. 2020, *ApJ*, 903, 112, doi: [10.3847/1538-4357/abbc1c](https://doi.org/10.3847/1538-4357/abbc1c)
- de Jong, R. S., Bellido-Tirado, O., Chiappini, C., et al. 2012, in *Society of Photo-Optical Instrumentation Engineers (SPIE) Conference Series*, Vol. 8446, *Ground-based and Airborne Instrumentation for Astronomy IV*, ed. I. S. McLean, S. K. Ramsay, & H. Takami, 84460T, doi: [10.1117/12.926239](https://doi.org/10.1117/12.926239)
- Del Zanna, G., & DeLuca, E. E. 2018, *ApJ*, 852, 52, doi: [10.3847/1538-4357/aa9edf](https://doi.org/10.3847/1538-4357/aa9edf)
- Dimitrijević, M. S., Popović, L. Č., Kovačević, J., Dačić, M., & Ilić, D. 2007, *MNRAS*, 374, 1181, doi: [10.1111/j.1365-2966.2006.11238.x](https://doi.org/10.1111/j.1365-2966.2006.11238.x)
- Dojčinović, I., Kovačević-Dojčinović, J., & Popović, L. Č. 2023, *Advances in Space Research*, 71, 1219, doi: [10.1016/j.asr.2022.04.041](https://doi.org/10.1016/j.asr.2022.04.041)
- Dong, X., Wang, T., Wang, J., et al. 2008, *MNRAS*, 383, 581, doi: [10.1111/j.1365-2966.2007.12560.x](https://doi.org/10.1111/j.1365-2966.2007.12560.x)
- Dong, X.-B., Wang, J.-G., Ho, L. C., et al. 2011, *ApJ*, 736, 86, doi: [10.1088/0004-637X/736/2/86](https://doi.org/10.1088/0004-637X/736/2/86)
- Du, P., Wang, J.-M., Hu, C., et al. 2016, *ApJL*, 818, L14, doi: [10.3847/2041-8205/818/1/L14](https://doi.org/10.3847/2041-8205/818/1/L14)
- Frederick, S., Gezari, S., Graham, M. J., et al. 2021, *ApJ*, 920, 56, doi: [10.3847/1538-4357/ac110f](https://doi.org/10.3847/1538-4357/ac110f)
- Fuhr, J. R., Martin, G. A., Wlese, W. L., & Younger, S. M. 1981, *Journal of Physical and Chemical Reference Data*, 10, 305, doi: [10.1063/1.555644](https://doi.org/10.1063/1.555644)
- Garcia-Rissmann, A., Rodríguez-Ardila, A., Sigut, T. A. A., & Pradhan, A. K. 2012, *ApJ*, 751, 7, doi: [10.1088/0004-637X/751/1/7](https://doi.org/10.1088/0004-637X/751/1/7)
- Gaskell, C. M. 2017, *MNRAS*, 467, 226, doi: [10.1093/mnras/stx094](https://doi.org/10.1093/mnras/stx094)
- Gaskell, M., Thakur, N., Tian, B., & Saravanan, A. 2022, *Astronomische Nachrichten*, 343, e210112, doi: [10.1002/asna.20210112](https://doi.org/10.1002/asna.20210112)
- Gezari, S. 2021, *ARA&A*, 59, 21, doi: [10.1146/annurev-astro-111720-030029](https://doi.org/10.1146/annurev-astro-111720-030029)
- . 2022, *Nature Astronomy*, doi: [10.1038/s41550-022-01859-w](https://doi.org/10.1038/s41550-022-01859-w)
- Greene, J. E., & Ho, L. C. 2005, *ApJ*, 630, 122, doi: [10.1086/431897](https://doi.org/10.1086/431897)
- Guo, H., Liu, X., Shen, Y., et al. 2019, *MNRAS*, 482, 3288, doi: [10.1093/mnras/sty2920](https://doi.org/10.1093/mnras/sty2920)
- Guo, H., Shen, Y., & Wang, S. 2018, *PyQSOFit*: Python code to fit the spectrum of quasars, *Astrophysics Source Code Library*, record ascl:1809.008. <http://ascl.net/1809.008>
- Hönig, S. F., Kishimoto, M., Antonucci, R., et al. 2012, *ApJ*, 755, 149, doi: [10.1088/0004-637X/755/2/149](https://doi.org/10.1088/0004-637X/755/2/149)
- Ilić, D., Popović, L. Č., La Mura, G., Ciroi, S., & Rafanelli, P. 2012, *A&A*, 543, A142, doi: [10.1051/0004-6361/201219299](https://doi.org/10.1051/0004-6361/201219299)
- Ilić, D., Shapovalova, A. I., Popović, L. Č., et al. 2017, *Frontiers in Astronomy and Space Sciences*, 4, 12, doi: [10.3389/fspas.2017.00012](https://doi.org/10.3389/fspas.2017.00012)
- Ilić, D., Oknyansky, V., Popović, L. Č., et al. 2020, *A&A*, 638, A13, doi: [10.1051/0004-6361/202037532](https://doi.org/10.1051/0004-6361/202037532)
- Ivezić, Ž., Kahn, S. M., Tyson, J. A., et al. 2019, *ApJ*, 873, 111, doi: [10.3847/1538-4357/ab042c](https://doi.org/10.3847/1538-4357/ab042c)

- Kaspi, S., Smith, P. S., Netzer, H., et al. 2000, *ApJ*, 533, 631, doi: [10.1086/308704](https://doi.org/10.1086/308704)
- Kormendy, J., & Ho, L. C. 2013, *ARA&A*, 51, 511, doi: [10.1146/annurev-astro-082708-101811](https://doi.org/10.1146/annurev-astro-082708-101811)
- Kovacevic, A., Zekovic, V., Ilic, D., et al. 2022, *Publications of the Astronomical Society “Rudjer Boskovic”*, 22, 231
- Kovačević, J., Popović, L. Č., & Dimitrijević, M. S. 2010, *ApJS*, 189, 15, doi: [10.1088/0067-0049/189/1/15](https://doi.org/10.1088/0067-0049/189/1/15)
- Kovačević-Dojčinović, J., Dojčinović, I., Lakićević, M., & Popović, L. Č. 2022, *A&A*, 659, A130, doi: [10.1051/0004-6361/202141043](https://doi.org/10.1051/0004-6361/202141043)
- Kovačević-Dojčinović, J., & Popović, L. Č. 2015, *ApJS*, 221, 35, doi: [10.1088/0067-0049/221/2/35](https://doi.org/10.1088/0067-0049/221/2/35)
- Kramida, A., Yu. Ralchenko, Reader, J., & and NIST ASD Team. 2022, NIST Atomic Spectra Database (ver. 5.10), [Online]. Available: <https://physics.nist.gov/asd> [2023, February 3]. National Institute of Standards and Technology, Gaithersburg, MD.
- Kuehn, C. A., Baldwin, J. A., Peterson, B. M., & Korista, K. T. 2008, *ApJ*, 673, 69, doi: [10.1086/524183](https://doi.org/10.1086/524183)
- La Mura, G., Popović, L. Č., Ciroi, S., Rafanelli, P., & Ilić, D. 2007, *ApJ*, 671, 104, doi: [10.1086/522821](https://doi.org/10.1086/522821)
- Landt, H., Bentz, M. C., Ward, M. J., et al. 2008, *ApJS*, 174, 282, doi: [10.1086/522373](https://doi.org/10.1086/522373)
- Liu, H.-Y., Liu, W.-J., Dong, X.-B., et al. 2019, *ApJS*, 243, 21, doi: [10.3847/1538-4365/ab298b](https://doi.org/10.3847/1538-4365/ab298b)
- Lu, K.-X., Zhao, Y., Bai, J.-M., & Fan, X.-L. 2019, *MNRAS*, 483, 1722, doi: [10.1093/mnras/sty3229](https://doi.org/10.1093/mnras/sty3229)
- Marinello, M., Rodríguez-Ardila, A., Garcia-Rissmann, A., Sigut, T. A. A., & Pradhan, A. K. 2016, *ApJ*, 820, 116, doi: [10.3847/0004-637X/820/2/116](https://doi.org/10.3847/0004-637X/820/2/116)
- Marinello, M., Rodríguez-Ardila, A., Marziani, P., Sigut, A., & Pradhan, A. 2020, *MNRAS*, 494, 4187, doi: [10.1093/mnras/staa934](https://doi.org/10.1093/mnras/staa934)
- Marziani, P., del Olmo, A., Perea, J., D’Onofrio, M., & Panda, S. 2020, *Atoms*, 8, 94, doi: [10.3390/atoms8040094](https://doi.org/10.3390/atoms8040094)
- Marziani, P., del Olmo, A., D’Onofrio, M., et al. 2018a, in *Revisiting Narrow-Line Seyfert 1 Galaxies and their Place in the Universe*, 2. <https://arxiv.org/abs/1807.03003>
- Marziani, P., Dultzin, D., Sulentic, J. W., et al. 2018b, *Frontiers in Astronomy and Space Sciences*, 5, 6, doi: [10.3389/fspas.2018.00006](https://doi.org/10.3389/fspas.2018.00006)
- Marziani, P., Bon, E., Bon, N., et al. 2022, *Astronomische Nachrichten*, 343, e210082, doi: [10.1002/asna.20210082](https://doi.org/10.1002/asna.20210082)
- Netzer, H. 1980, *ApJ*, 236, 406, doi: [10.1086/157757](https://doi.org/10.1086/157757)
- . 2013, *The Physics and Evolution of Active Galactic Nuclei*
- . 2020, *MNRAS*, 494, 1611, doi: [10.1093/mnras/staa767](https://doi.org/10.1093/mnras/staa767)
- Osterbrock, D. E., & Ferland, G. J. 2006, *Astrophysics of gaseous nebulae and active galactic nuclei*
- Padovani, P., Alexander, D. M., Assef, R. J., et al. 2017, *A&A Rv*, 25, 2, doi: [10.1007/s00159-017-0102-9](https://doi.org/10.1007/s00159-017-0102-9)
- Panda, S., Marziani, P., & Czerny, B. 2019, *ApJ*, 882, 79, doi: [10.3847/1538-4357/ab3292](https://doi.org/10.3847/1538-4357/ab3292)
- Park, D., Barth, A. J., Ho, L. C., & Laor, A. 2022, *ApJS*, 258, 38, doi: [10.3847/1538-4365/ac3f3e](https://doi.org/10.3847/1538-4365/ac3f3e)
- Paul, B., Winkler, H., & Potter, S. 2022, *MNRAS*, 516, 2374, doi: [10.1093/mnras/stac2028](https://doi.org/10.1093/mnras/stac2028)
- Penston, M. V. 1987, *MNRAS*, 229, 1P, doi: [10.1093/mnras/229.1.1P](https://doi.org/10.1093/mnras/229.1.1P)
- Petrushevskaya, T., Leloudas, G., Ilić, D., et al. 2023, *A&A*, 669, A140, doi: [10.1051/0004-6361/202244623](https://doi.org/10.1051/0004-6361/202244623)
- Popović, L. Č. 2003, *ApJ*, 599, 140, doi: [10.1086/376401](https://doi.org/10.1086/376401)
- . 2020, *Open Astronomy*, 29, 1, doi: [10.1515/astro-2020-0003](https://doi.org/10.1515/astro-2020-0003)
- Popović, L. Č., Kovačević-Dojčinović, J., & Marčeta-Mandić, S. 2019, *MNRAS*, 484, 3180, doi: [10.1093/mnras/stz157](https://doi.org/10.1093/mnras/stz157)
- Popović, L. Č., Mediavilla, E., Bon, E., & Ilić, D. 2004, *A&A*, 423, 909, doi: [10.1051/0004-6361:20034431](https://doi.org/10.1051/0004-6361:20034431)
- Rakić, N. 2022, *MNRAS*, 516, 1624, doi: [10.1093/mnras/stac2259](https://doi.org/10.1093/mnras/stac2259)
- Rakshit, S., Stalin, C. S., Chand, H., & Zhang, X.-G. 2017, *ApJS*, 229, 39, doi: [10.3847/1538-4365/aa6971](https://doi.org/10.3847/1538-4365/aa6971)
- Rakshit, S., Stalin, C. S., & Kotilainen, J. 2020, *ApJS*, 249, 17, doi: [10.3847/1538-4365/ab99c5](https://doi.org/10.3847/1538-4365/ab99c5)
- Richards, G. T., Lacy, M., Storrie-Lombardi, L. J., et al. 2006, *ApJS*, 166, 470, doi: [10.1086/506525](https://doi.org/10.1086/506525)
- Rudy, R. J., Mazuk, S., Puetter, R. C., & Hamann, F. 2000, *ApJ*, 539, 166, doi: [10.1086/309222](https://doi.org/10.1086/309222)
- Sarkar, A., Ferland, G. J., Chatzikos, M., et al. 2021, *ApJ*, 907, 12, doi: [10.3847/1538-4357/abcaa6](https://doi.org/10.3847/1538-4357/abcaa6)
- Schindler, J.-T. 2022, *Sculptor: Interactive modeling of astronomical spectra*, Astrophysics Source Code Library, record ascl:2202.018. <http://ascl.net/2202.018>
- Schlegel, D. J., Finkbeiner, D. P., & Davis, M. 1998, *ApJ*, 500, 525, doi: [10.1086/305772](https://doi.org/10.1086/305772)
- Shapovalova, A. I., Popović, L. Č., Burenkov, A. N., et al. 2012, *ApJS*, 202, 10, doi: [10.1088/0067-0049/202/1/10](https://doi.org/10.1088/0067-0049/202/1/10)
- Shen, Y., & Ho, L. C. 2014, *Nature*, 513, 210, doi: [10.1038/nature13712](https://doi.org/10.1038/nature13712)
- Shen, Y., Richards, G. T., Strauss, M. A., et al. 2011, *ApJS*, 194, 45, doi: [10.1088/0067-0049/194/2/45](https://doi.org/10.1088/0067-0049/194/2/45)
- Shen, Y., Hall, P. B., Horne, K., et al. 2019, *ApJS*, 241, 34, doi: [10.3847/1538-4365/ab074f](https://doi.org/10.3847/1538-4365/ab074f)
- Sigut, T. A. A., & Pradhan, A. K. 1998, *ApJL*, 499, L139, doi: [10.1086/311369](https://doi.org/10.1086/311369)
- . 2003, *ApJS*, 145, 15, doi: [10.1086/345498](https://doi.org/10.1086/345498)
- Sigut, T. A. A., Pradhan, A. K., & Nahar, S. N. 2004, *ApJ*, 611, 81, doi: [10.1086/422027](https://doi.org/10.1086/422027)

- Smartt, S. J., Valenti, S., Fraser, M., et al. 2015, *A&A*, 579, A40, doi: [10.1051/0004-6361/201425237](https://doi.org/10.1051/0004-6361/201425237)
- Smee, S. A., Gunn, J. E., Uomoto, A., et al. 2013, *AJ*, 146, 32, doi: [10.1088/0004-6256/146/2/32](https://doi.org/10.1088/0004-6256/146/2/32)
- Stalevski, M., Asmus, D., & Tristram, K. R. W. 2017, *MNRAS*, 472, 3854, doi: [10.1093/mnras/stx2227](https://doi.org/10.1093/mnras/stx2227)
- Sulentic, J. W., Marziani, P., & Dultzin-Hacyan, D. 2000, *ARA&A*, 38, 521, doi: [10.1146/annurev.astro.38.1.521](https://doi.org/10.1146/annurev.astro.38.1.521)
- Sulentic, J. W., Marziani, P., Zamanov, R., et al. 2002, *ApJL*, 566, L71, doi: [10.1086/339594](https://doi.org/10.1086/339594)
- The MSE Science Team, Babusiaux, C., Bergemann, M., et al. 2019, arXiv e-prints, arXiv:1904.04907. <https://arxiv.org/abs/1904.04907>
- Tsuzuki, Y., Kawara, K., Yoshii, Y., et al. 2006, *ApJ*, 650, 57, doi: [10.1086/506376](https://doi.org/10.1086/506376)
- van Groningen, E. 1993, *A&A*, 272, 25
- Vanden Berk, D. E., Richards, G. T., Bauer, A., et al. 2001, *AJ*, 122, 549, doi: [10.1086/321167](https://doi.org/10.1086/321167)
- Vanden Berk, D. E., Shen, J., Yip, C.-W., et al. 2006, *AJ*, 131, 84, doi: [10.1086/497973](https://doi.org/10.1086/497973)
- Verner, E. M., Verner, D. A., Korista, K. T., et al. 1999, *ApJS*, 120, 101, doi: [10.1086/313171](https://doi.org/10.1086/313171)
- Véron-Cetty, M. P., Joly, M., & Véron, P. 2004, *A&A*, 417, 515, doi: [10.1051/0004-6361:20035714](https://doi.org/10.1051/0004-6361:20035714)
- Vestergaard, M., & Peterson, B. M. 2005, *ApJ*, 625, 688, doi: [10.1086/429791](https://doi.org/10.1086/429791)
- Vestergaard, M., & Wilkes, B. J. 2001, *ApJS*, 134, 1, doi: [10.1086/320357](https://doi.org/10.1086/320357)
- Wang, J., Wei, J. Y., & He, X. T. 2005, *A&A*, 436, 417, doi: [10.1051/0004-6361:20042014](https://doi.org/10.1051/0004-6361:20042014)
- Wills, B. J., Netzer, H., & Wills, D. 1985, *ApJ*, 288, 94, doi: [10.1086/162767](https://doi.org/10.1086/162767)
- Xiao, T., Barth, A. J., Greene, J. E., et al. 2011, *ApJ*, 739, 28, doi: [10.1088/0004-637X/739/1/28](https://doi.org/10.1088/0004-637X/739/1/28)
- Yip, C. W., Connolly, A. J., Szalay, A. S., et al. 2004a, *AJ*, 128, 585, doi: [10.1086/422429](https://doi.org/10.1086/422429)
- Yip, C. W., Connolly, A. J., Vanden Berk, D. E., et al. 2004b, *AJ*, 128, 2603, doi: [10.1086/425626](https://doi.org/10.1086/425626)